Mathematical relationships between spinal motoneuron properties

Arnault H Caillet[1], Andrew TM Phillips[1], Dario Farina[2†], Luca Modenese[1,3*†]

[1]Department of Civil and Environmental Engineering, Imperial College London, London, United Kingdom; [2]Department of Bioengineering, Imperial College London, London, United Kingdom; [3]Graduate School of Biomedical Engineering, University of New South Wales, Sydney, Australia

Abstract Our understanding of the behaviour of spinal alpha-motoneurons (MNs) in mammals partly relies on our knowledge of the relationships between MN membrane properties, such as MN size, resistance, rheobase, capacitance, time constant, axonal conduction velocity, and afterhyperpolarization duration. We reprocessed the data from 40 experimental studies in adult cat, rat, and mouse MN preparations to empirically derive a set of quantitative mathematical relationships between these MN electrophysiological and anatomical properties. This validated mathematical framework, which supports past findings that the MN membrane properties are all related to each other and clarifies the nature of their associations, is besides consistent with the Henneman's size principle and Rall's cable theory. The derived mathematical relationships provide a convenient tool for neuroscientists and experimenters to complete experimental datasets, explore the relationships between pairs of MN properties never concurrently observed in previous experiments, or investigate inter-mammalian-species variations in MN membrane properties. Using this mathematical framework, modellers can build profiles of inter-consistent MN-specific properties to scale pools of MN models, with consequences on the accuracy and the interpretability of the simulations.

*For correspondence:
l.modenese@unsw.edu.au

[†]These authors contributed equally to this work and share the senior authorship

Editor's evaluation

This article will be of interest to scientists studying the contribution of motoneuron behaviour to motor control as well as anyone interested in the relation between neuron morphology, intrinsic properties, and neuron behaviour. The authors have distilled decades of research on motoneuron properties into a set of mathematical relationships that can guide both experimentalists and modellers interested in developing realistic models of populations of motoneurons. In fact, Caillet et al. present a data-driven regression analysis to infer the relationships between morphological and electrophysiological measures from spinal motor neurons in different animal species. Finally, the authors emphasize the value of this approach, but also carefully consider its limitations, including inter-study variability and limited sample sizes in the experimental datasets used to derive the relationships between multiple intrinsic properties.

Introduction

Assessing the morphological and electrophysiological properties of individual spinal alpha-motoneurons (MNs) is crucial for understanding their recruitment and discharge behaviour, and exploring the neuro-mechanical interplay that controls voluntary motion in mammals. As measured in individual spinal MNs in experimental studies and reported in review papers (*Henneman, 1981*; *Burke, 1981*; *Binder et al., 1996*; *Powers and Binder, 2001*; *Olinder et al., 2006*; *Heckman and Enoka, 2012*), significant correlations exist in mammalian MN pools between the MN morphological and/or electrophysiological properties reported

eLife digest Muscles receive their instructions through electrical signals carried by tens or hundreds of cells connected to the command centers of the body. These 'alpha-motoneurons' have various sizes and electrical characteristics which affect how they transmit signals. Previous experiments have shown that these properties are linked; for instance, larger motoneurons transfer electrical signals more quickly. The exact nature of the mathematical relationships between these characteristics, however, remains unclear. This limits our understanding of the behaviour of motoneurons from experimental data.

To identify the equations linking eight motoneuron properties, Caillet et al. analysed published datasets from experimental studies on cat motoneurons. This approach uncovered simple mathematical associations: in fact, only one characteristic needs to be measured experimentally to calculate all the other properties. The relationships identified were also consistent with previously accepted approaches for modelling motoneuron activity. Caillet et al. then validated this mathematical framework with data from studies on rodents, showing that some of the equations hold true for different mammals.

This work offers a quick and easy way for researchers to calculate the characteristics of a motoneuron based on a single observation. This will allow non-measured properties to be added to experimental datasets, and it could help to uncover the diversity of motoneurons at work within a population.

in *Table 1*. For example, the soma size (D_{soma}) and the current threshold for spike initiation (I_{th}) of an MN are both positively correlated to the axonal conduction velocity (ACV) and afterhyperpolarization duration (AHP). Also, I_{th} decreases with increasing input resistance (R) and AHP, R is negatively correlated to ACV and D_{soma}, and ACV varies inversely with AHP. Besides supporting and sequentially leading to extensions of the Henneman's size principle (*Henneman, 1957*; *Wuerker et al., 1965*; *Henneman et al., 1965a*; *Henneman et al., 1965b*; *Henneman et al., 1974*; *Henneman, 1981*; *Henneman, 1985*), these empirical associations find strong consistency with Rall's theoretical approach of representing the soma and the dendritic trees of MNs as an equivalent cylinder (*Rall, 1977*; *Rall et al., 1992*; *Powers and Binder, 2001*). In such case, MNs behave like resistive-capacitive (RC) circuits, as successfully simulated with computational RC models (*Izhikevich, 2004*; *Dong et al., 2011*; *Negro et al., 2016*; *Teeter et al., 2018*), that rely on further property associations, such as the MN membrane time constant τ precisely equalling the product of the MN membrane-specific capacitance C_m and resistivity R_m ($\tau = R_m C_m$).

Yet, because the empirical correlations between MN properties were obtained from scattered data from individual experimental studies, the quantitative mathematical associations between the MN properties reported in *Table 1*, beyond their aforementioned global relative variations, remain unclear. For example, the negative correlation between R and ACV was described in the literature with linear (*Fleshman et al., 1981*), exponential (*Burke, 1968*) or power relationships (*Kernell, 1966*; *Kernell and Zwaagstra, 1981*; *Ulfhake and Kellerth, 1984*; *Gustafsson and Pinter, 1984a*), while *Zwaagstra and Kernell, 1980* reported for this association a slope twice greater than *Gustafsson and Pinter, 1984a* in the double-logarithmic space. This makes it difficult to reconcile the conclusions of multiple empirical studies that investigated different property associations. For example, *Burke, 1968* and *Zwaagstra and Kernell, 1980*, respectively, proposed exponential $R - ACV$ and linear $ACV - AHP$ associations, suggesting a hybrid exponential relationship between R and AHP, that is different from the power $R - AHP$ relationship directly reported by *Ulfhake and Kellerth, 1984*. These divergences between studies are a major limitation for our understanding of the associations and the distribution of MN properties in an MN pool, which cannot be directly investigated experimentally either, as measuring multiple MN morphometric properties in vitro and electrophysiological properties in vivo for a large sample of MNs is challenging.

Here, we reprocessed and merged the published data from 19 available experimental studies in adult cat preparations to derive and validate a unique set of mathematical power relationships between all pairs of the MN morphometric and electrophysiological cat properties listed in *Table 1*. The significance of these quantitative relationships, which are consistent with the conclusions from Rall's cable theory, supports the notion that the properties reported in *Table 1* are all associated to each other. The uniqueness of these mathematical relationships tackles the aforementioned inter-study variability in describing the data and clarifies our understanding of the quantitative association between spinal MN properties, including for pairs

Table 1. The motoneuron (MN) and muscle unit (mU) properties investigated in this study with their notations and SI base units.

S_{MN} is the size of the MN. As reproduced in *Table 2*, the MN size S_{MN} is adequately described by measures of the MN surface area S_{neuron} and the soma diameter D_{soma}. R and R_m define the MN-specific electrical resistance properties of the MN and set the value of the MN-specific current threshold I_{th} (*Binder et al., 1996*; *Powers and Binder, 2001*; *Heckman and Enoka, 2012*). C and C_m (constant among the MN pool) define the capacitance properties of the MN and contribute to the definition of the MN membrane time constant τ (*Gustafsson and Pinter, 1984a*; *Zengel et al., 1985*). ΔV_{th} is the amplitude of the membrane voltage depolarization threshold relative to resting state required to elicit an action potential. I_{th} is the corresponding electrical current causing a membrane depolarization of ΔV_{th}. AHP duration is defined in most studies as the duration between the action potential onset and the time at which the MN membrane potential meets the resting state after being hyperpolarized. ACV is the axonal conduction velocity of the elicited action potentials on the MN membrane. S_{mU} is the size of the mU. As indicated in *Table 2*, the mU size S_{mU} is adequately described by measures of (1) the sum of the cross-sectional areas (CSAs) of the fibres composing the mU CSA^{tot}, (2) the mean fibre CSA CSA^{mean}, (3) the innervation ratio IR, that is, the number of innervated fibres constituting the mU, and (4) the mU tetanic force F^{tet}. F^{tw} is the MU twitch force.

	Properties	Notation	Unit
	Size: Neuron surface area Soma diameter	S_{MN} S_{neuron} D_{soma}	 $[\mathrm{m^2}]$ $[\mathrm{m}]$
	Resistance	R	$[\Omega]$
	Specific resistance per unit area	R_m	$[\Omega \cdot \mathrm{m^2}]$
	Capacitance	C	$[\mathrm{F}]$
	Specific capacitance per unit area	C_m	$[\mathrm{F} \cdot \mathrm{m^{-2}}]$
	Time constant	τ	$[\mathrm{s}]$
	Rheobase (current recruitment threshold)	I_{th}	$[\mathrm{A}]$
	Voltage threshold	ΔV_{th}	$[\mathrm{V}]$
	Afterhyperpolarization duration	AHP	$[\mathrm{s}]$
MN properties	Axonal conduction velocity	ACV	$[\mathrm{m} \cdot \mathrm{s^{-1}}]$
	Size:	S_{mU}	
	Total fibre cross-sectional area	CSA^{tot}	$[\mathrm{m^2}]$
	Mean fibre cross-sectional area	CSA^{mean}	$[\mathrm{m^2}]$
	Innervation ratio	IR	$[]$
	Tetanic force	F^{tet}	$[\mathrm{N}]$
mU properties	Twitch force	F^{tw}	$[\mathrm{N}]$

of properties never simultaneously measured in experiments. These relationships also provide a convenient mathematical framework for modellers for the derivation of appropriate and consistent MN profiles of MN-specific morphometric and electrophysiological properties for the realistic scaling of pools of computational models of MNs, improving the interpretability of model predictions. Using the relationships, experimenters can readily complete their datasets by deriving MN-specific values, which are representative of the literature, for the MN properties that were not experimentally measured.

After deriving the mathematical framework from cat data, we then demonstrate that the normalized cat relationships apply to other mammals by validating them with data from nine adult rat and mouse

electrophysiological studies in vivo. This approach helps better understanding the inter-mammalian-species variations in MN properties. Finally, using additional correlations obtained between some MN and muscle unit (mU) properties from 14 mammal studies, we discuss the empirical relationships obtained between MN properties in the context of the Henneman's size principle.

Methods
Selected studies reporting processable adult mammal data
Identification of the selected studies

To optimize inter-study consistency, we only selected studies that concurrently measured at least two of the morphometric and/or electrophysiological properties reported in *Table 1* in individual spinal alpha-MNs of healthy adult cats, rats, and mice. To build an extensive set of relevant studies so that the mathematical relationships derived in this study describe a maximum of the data published in the literature, the output of the systematic analysis provided in *Highlander et al., 2020* was screened and used for a further search by reference lists. Among the retrieved studies, larval and postnatal specimens were disregarded because of the pronounced age-related variance (*Highlander et al., 2020*) in the mean values of the electrophysiological properties listed in *Table 1*, which corroborates the non-extrapolability of neonatal neuronal circuitry to older ages (*Song et al., 2006*; *Carp et al., 2008*; *Nakanishi and Whelan, 2010*; *Mitra and Brownstone, 2012*). Due to the nonlinear inter-species scalability of the spinal alpha-MN electrophysiological and morphometric properties (*Manuel et al., 2019*) and a pronounced variance in the inter-species mean values (*Highlander et al., 2020*), non-mammalian species were also disregarded, while the retained data from cats, rats, and mice were processed separately. *Highlander et al., 2020* also report an 'unexplained' variance in the mean electrophysiological property values reported between studies investigating specimens of the same species, sex, and age, which may be explained by the differences between in vivo and in vitro protocols (*Carp et al., 2008*). For this reason, only studies measuring the electrophysiological properties in vivo were considered, while most in vitro studies had already been disregarded at this stage as dominantly performed on neonatal specimens due to experimental constraints (*Manuel et al., 2009*; *Mitra and Brownstone, 2012*). As all but two of the remaining selected studies focussed on lumbosacral MNs, the final set of considered publications was constrained to MNs innervating hindlimb muscles to improve inter-study consistency. From a preliminary screening of the final set of selected studies, it was finally found that relatively more cat studies (19) were obtained than rat (9) and mouse (4) studies, while the cat studies also investigated more pairs of morphometric and electrophysiological properties. The mathematical relationships sought in this article between MN properties were thus derived from the cat data reported in the selected studies, and then validated for extrapolation to rat and mouse data.

Selected studies providing cat data: Experimental approaches

The 19 selected studies focussing on cats that were included in this work were published between 1966 and 2001. They applied similar experimental protocols to measure the morphometric and electrophysiological properties reported in *Table 1*. All the selected studies performing morphometric measurements injected in vitro the recorded MNs intracellularly with horseradish peroxidase (HRP) tracer by applying a continuous train of anodal current pulses. The spinal cord was eventually sliced frozen or at room temperature with a microtome or a vibratome and the MN morphometry was investigated. All morphometric measurements were manually performed, and the MN compartments (soma, dendrites, axon) approximated by simple geometrical shapes, yielding some experimental limitations discussed later in 'Methods' and Appendix 1.

To measure the electrophysiological properties, animals were anaesthetized, immobilized, and kept under artificial breathing. Hindlimb muscles of interest were dissected free, and their nerves were mounted onto stimulating electrodes, while maintaining body temperature between 35 and 38°C. After a laminectomy was performed over the lumbosacral region of the spinal cord, the MNs were identified by antidromic invasion following electrical stimulation of the corresponding muscle nerves. All selected cat studies reported the use of electrodes having stable resistances and being able to pass currents up to 10 nA without evident polarization or rectification. Some aspects of the experimental protocol however diverged between the selected studies, such as the age and the sex of the group of adult cats, the size population of cats and recorded MNs, the muscles innervated by the recorded MNs, the means of anaesthesia, the level of oxygen, and whether the spinal dorsal roots were severed (*Kernell, 1966*; *Burke, 1968*; *Barrett and Crill, 1974*; *Fleshman et al., 1981*; *Gustafsson and Pinter, 1984a*; *Gustafsson and Pinter, 1984b*; *Zengel et al., 1985*;

Foehring et al., 1987), the complete surrounding hindlimbs were denervated (*Burke, 1968*; *Kernell and Zwaagstra, 1981*), or the spinal cord was transected (*Burke, 1968*; *Krawitz et al., 2001*).

In all the selected cat studies, ACV was calculated as the ratio of the conduction distance and the anti-dromic spike latency between the stimulation site and the ventral root entry. The studies however did not report how the nerve length was estimated. AHP was measured using brief suprathreshold antidromic stim-ulations as the time interval between the spike onset to when the voltage deflection of the hyperpolarizing phase returned to the prespike membrane potential. In all studies, I_{th} was obtained as the minimal intensity of a 50–100-ms-long depolarizing rectangular current pulse required to produce regular discharges. I_{th} was obtained with a trial-and-error approach, slowly increasing the intensity of the pulse. The selected studies did not report any relevant source of inaccuracy in measuring ACV, AHP, and I_{th}. The studies measured R using the spike height method (*Frank and Fuortes, 1956*). In brief, small (1–5 nA) depolarizing and/or hyperpolarizing current pulses (I_{in}) of 15–100 ms duration were injected through a Wheatstone bridge circuit in the intracellular microelectrode amplifier, and the subsequent change in the amplitude of the membrane voltage potential (V_m) was reported in steady-state $V_m - I_{in}$ plots. In all studies, R was obtained by calculating the slope of the linear part of the $V_m - I_{in}$ plots near resting membrane potential by analogy with Ohm's law. It is worth noting for inter-study variability that depolarizing pulses return slightly higher R values than hyperpolarizing currents (*Sasaki, 1991*). To measure the membrane time constant τ, all the selected studies analysed the transient voltage responses (V_m) to weak (1–12 nA), brief (0.5 ms), or long (15–100 ms) hyper-polarizing current pulses. Both brief- and long-pulse approaches were reported to provide similar results for the estimation of τ (*Ulfhake and Kellerth, 1984*). Considering MNs as equivalent isopotential cables, the membrane time constant τ was identified in all studies as the longest time constant when modelling the measured voltage transient response to a current pulse as the sum of weighted time-dependent exponential terms (*Rall, 1969*; *Rall, 1977*; *Powers and Binder, 2001*). Semi-logarithmic plots of the time history of the voltage transient V_m or of its time derivative $\frac{dV_m}{dt}$ were drawn, and a straight line was fit by eye to the linear tail of the resulting plot (*Fleshman et al., 1988*), the slope of which was τ. A graphical 'peeling' process (*Rall, 1969*) was undertaken to recover the first equalizing time constant τ_1, required to estimate the electronic length (L) of Rall's equivalent cylinder representation of the MN and the MN membrane capacitance with Rall's equations (*Rall, 1969*; *Rall, 1977*; *Gustafsson and Pinter, 1984b*; *Powers and Binder, 2001*):

$$L \approx \left[\frac{\pi}{\left(\frac{\tau}{\tau_1} - 1 \right)} \right]^{\frac{1}{2}}$$

$$C = \frac{\tau}{R} \cdot \frac{L}{\tanh(L)}$$

These electrophysiological measurements were reported to be subject to three main experimental sources of inaccuracy. First, a variable membrane 'leak' conductance, which can be estimated from the ratio of two parameters obtained from the 'peeling' process (*Gustafsson and Pinter, 1984b*), arises from the imperfect seal around the recording micropipette (*Ulfhake and Kellerth, 1984*; *Gustafsson and Pinter, 1984b*; *Pinter and Vanden Noven, 1989*). As reviewed in *Powers and Binder, 2001* and *Olinder et al., 2006*, this 'leak' can affect the measurements of all the properties, notably underestimating the values of R and τ and overestimating those of C. However, this 'leak' is probably not of major significance in the cells of large spike amplitudes (*Gustafsson and Pinter, 1984b*), on which most of the selected studies focussed. Importantly, the membrane 'leak' is also not expected to affect the relations between the param-eters (*Gustafsson and Pinter, 1984b*).

Secondly, some nonlinearities (*Ito and Oshima, 1965*; *Burke and ten Bruggencate, 1971*; *Ulfhake and Kellerth, 1984*) in the membrane voltage response to input current steps arise near threshold because of the contribution of voltage-activated membrane conductances to the measured voltage decay (*Fleshman et al., 1988*). This contradicts the initial assumption of the MN membrane remaining passive to input current steps (*Rall, 1969*; *Burke and ten Bruggencate, 1971*). Because of this issue, the ends of the $V_m - I_{in}$ plot are curvilinear and can affect the estimation of R, while the transient voltage response to an input current pulse decays faster than exponentially (it undershoots) at the termination of the current injection, which makes it impossible to plot the entire course of $\ln(V(t))$ and challenges the graphical procedure taken to estimate τ (*Fleshman et al., 1988*). Therefore, some of the selected studies discarded all the MNs that displayed obvious large nonlinearity in the semi-logarithmic V–t or $\frac{dV}{dt}$-t plots (*Burke and ten Bruggencate, 1971*). The membrane nonlinearities can be corrected by adding a constant voltage to the entire trace (*Fleshman et al., 1988*) or by considering the three time-constant

model of *Ito and Oshima, 1965* to approximate and subtract to the voltage signal the membrane potential change produced by the current steps. However, none of the selected studies performed such corrections, potentially yielding a systematic underestimation of the values of R and τ (*Gustafsson and Pinter, 1984b*; *Zengel et al., 1985*; *Powers and Binder, 2001*). Yet, this systematic error for R, which should not contribute to inter-study variability, is expected to remain low because the selected studies used input current pulses of low strength (*Ulfhake and Kellerth, 1984*) and measured R from the linear part of the I–V plots near the resting membrane potential where no membrane nonlinearity is expected to occur. This systematic error may also not affect the distribution of recorded R values, as displayed in *Zengel et al., 1985*. *Zengel et al., 1985* besides corrected for the membrane nonlinearities with the three time-constant model approach of *Ito and Oshima, 1965* when measuring τ and returned values of τ around 40% higher than the other selected studies. However, this systematic discrepancy is expected to disappear with the normalization of the datasets described in the following, as the reported normalized distributions of τ are very similar between the selected studies (see density histogram for the $\{\tau; R\}$ dataset in *Appendix 1—figure 1*). Thirdly, the highest source of inaccuracy and inter-study variability arises from the subjective fit 'by eye' of a straight line to the transient voltage when estimating τ (*Pinter and Vanden Noven, 1989*).

Overall, all the selected studies used similar experimental approaches to measure ACV, AHP, I_{th}, R, C, and τ, and little sources of inaccuracy and inter-study variability were identified.

Relationships between MN properties

For convenience, in the following, the notation $\{A; B\}$ refers to the pair of morphometric or electrophysiological MN properties A and B, with $A, B \in \{S_{MN}; ACV; AHP; R; I_{th}; C; \tau\}$, defined in *Table 1*. The selected studies generally provided clouds of data points for pairs $\{A; B\}$ of concurrently measured MN properties through scatter graphs. These plots were manually digitized using the online tool WebPlotDigitizer (*Ankit, 2020*). When a study did not provide such processable data – most reported the mean ± sd property values of the cohort of measured MNs – the corresponding author was contacted to obtain the raw data of the measured MN properties, following approval of data sharing. Upon reception of data, datasets of all possible $\{A; B\}$ pairs were created and included into the study.

Normalized space and choice of regression type

The sets of data retrieved from different cat studies for each property pair $\{A; B\}$ were merged into a 'global' dataset dedicated to that property pair. The $\{A; B\}$ data was also normalized for each study and transformed as a percentage of the maximum property value measured in the same study and normalized 'global' datasets were similarly created. A least-squares linear regression analysis was performed for the $\ln(A) - \ln(B)$ transformation of each global dataset yielding relationships of the type $\ln(A) = a \cdot \ln(B) + k$, which were then converted into power relationships of the type $A = k \cdot B^a$ (eq. 1). The adequacy of these global power trendlines and the statistical significance of the correlations were assessed with the coefficient of determination r^2 (squared value of the Pearson's correlation coefficient) and a threshold of 0.01 on the p-value of the regression analysis, respectively. For each $\{A; B\}$ pair, the normalized global datasets systematically returned both a higher r^2 and a lower p-value than the datasets of absolute $\{A; B\}$ values, in agreement with the 'unexplained' inter-experimental variance reported in *Highlander et al., 2020*. It was therefore decided to investigate the $\{A; B\}$ pairs of MN properties in the normalized space using the normalized global datasets to improve the cross-study analysis. For this preliminary analysis and the rest of the study, power regressions (eq. 1) were preferred to linear ($A = k + a \cdot B$) or exponential ($A = k \cdot e^{a \cdot B}$) regressions to maintain consistency with the mathematical structure of the equations from Rall's cable theory (*Rall, 1957*; *Rall, 1959*; *Rall, 1960*; *Powers and Binder, 2001*) and of other well-defined relationships, such as $R = k \cdot I_{th}^{-1}$. Also, a least-squares linear regression analysis was preliminary performed for each normalized experimental dataset and for its $\ln(A) - \ln(B)$ and $\ln(A) - B$ transformations, yielding linear, power, and exponential fits to the data. The power regressions overall returned $r^2 > 0.5$ for more experimental datasets than the linear and exponential fits (see *Appendix 1—table 1*). To avoid bias, power regressions were the only type of fit used in this study, despite a few datasets being more accurately fitted by linear or exponential regressions (the difference in the quality of the fit was very small in all cases). Other regression types, such as polynomial fits, were not justified by previous findings in the literature.

Global datasets and data variability

The data variability between the studies constituting the same global dataset $\{A; B\}$ was assessed by analysing the normalized distributions of the properties A and B with four metrics, which were the range of the measured data, the mean of the distribution, the coefficient of variation (CoV) calculated as the standard deviation (sd) divided by the mean of the distribution, and the ratio $\frac{Me}{Md}$ of the median and the mean of the distribution. The inter-study data variability in the $\{A; B\}$ global dataset was assessed by computing the $mean_g \pm sd_g$ across studies of each of the four metrics. Low variability between the data distributions from different studies was concluded if the normalized distributions (in percentage maximum value) returned similar values for the range, mean, CoV, and $\frac{Me}{Md}$ metrics, that is, when $sd_g < 10\%$ and $\frac{sd_g}{mean_g} < 0.15$ were obtained for all four metrics. In such case, the data distributions would respectively span over similar bandwidth length of the MU pool, be centred around similar mean values, and display similar data dispersion and similar skewness. The relative size of the experimental datasets reported by the selected studies constituting the same global datasets was also compared to assess their relative impact on the regression curves fitted to the global datasets. Then, the inter-study variability in associating the distributions of properties A and B was assessed by computing the 95% confidence interval of the linear model fitted to the global dataset $\{A; B\}$ in the log–log space, which yields the power regression $A = k \cdot B^a$. Low inter-study variability was considered if the value of a varied less than 0.4 in the confidence interval.

The variability of the data distribution of a property A between multiple global datasets $\{A; B\}$ was then assessed by computing the same four metrics as previously (range, mean, CoV, $\frac{Me}{Md}$) for each global dataset, and then computing the $mean_G \pm sd_G$ of each of the four metrics across the global datasets $\{A; B\}$. Low variability between the global datasets in the distribution of property A was considered if $sd_G < 10\%$ and $\frac{sd_G}{mean_G} < 0.15$ were obtained for all four metrics. If the inter-study and inter-global dataset variability was low, the global datasets were created and processed to derive the mathematical relationships between MN properties according to the procedure described below.

Size-dependent normalized relationships

From inspection of the considered cat studies, most of the investigated MN property pairs comprised either a direct measurement of MN size, noted as S_{MN} in this study, or another variable well-admitted to be strongly associated to size, such as ACV, AHP, or R. Accordingly, and consistently with Henneman's size principle, we identified S_{MN} as the reference MN property with respect to which relationships with the electrophysiological MN properties in *Table 1* were investigated. To integrate the data from all global normalized datasets into the final relationships, the MN properties in *Table 1* were processed in a step-by-step manner in the order ACV, AHP, R, I_{th}, C, τ, as reproduced in *Figure 1* for two arbitrary properties, to seek a 'final' power relationship of the type *eq.1* between each of them and S_{MN}. For each electrophysiological property A and each $\{A; B\}$ dataset, we considered two cases. If $B = S_{MN}$, the global dataset was not further processed as the electrophysiological property A was already related to MN size S_{MN} from experimental measurements. If $B \neq S_{MN}$, the global $\{A; B\}$ dataset was transformed into a new $\{A; S_{MN}\}$ dataset by converting the discrete values of B with the trendline regression $S_{MN} = k_d \cdot B^d$, which was obtained at a previous step of the data processing. With this dual approach, as many MN size-dependent $\{A; S_{MN}\}$ intermediary datasets as available $\{A; B\}$ global datasets were obtained for each property A. These size-dependent datasets were merged into a 'final' $\{A; S_{MN}\}$ dataset to which a least-squares linear regression analysis was performed for the $\ln(A) - \ln(S_{MN})$ transformation, yielding relationships of the type $\ln(A) = c \cdot \ln(S_{MN}) + k_c$, which were converted into the power relationships:

$$A = k_c \cdot S_{MN}^c$$

The adequacy of these final power trendlines and the statistical significance of the correlations were assessed identically to the $\{A; B\}$ relationships derived directly from normalized experimental data, using the coefficient of determination r^2 (squared value of the Pearson's correlation coefficient) and a threshold of 0.01 on the p-value of the regression analysis, respectively. If $r^2 > 0.3$ (i.e., $r > 0.55$) and p<0.01, another power trendline $S_{MN} = k_d \cdot A^d$ was fitted to the final dataset to describe the inverse relationship for $\{S_{MN}; A\}$ and used in the processing of the next-in-line property.
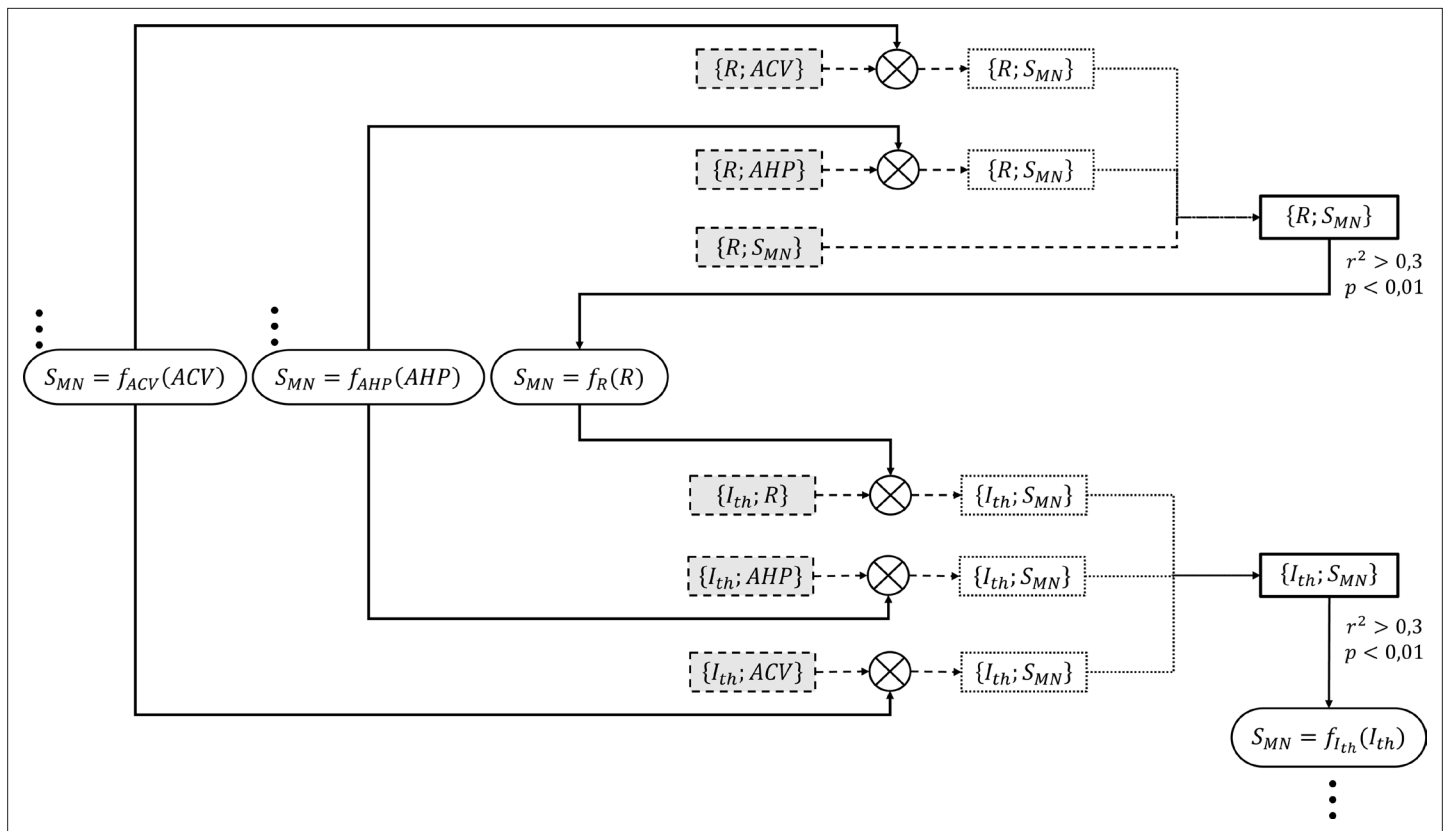
Figure 1. Detailed example for the process adopted to successively create the two final $\{R; S_{MN}\}$ and $\{I_{th}; S_{MN}\}$ datasets (right-side thick-solid contour rectangular boxes). These final datasets were obtained from respectively three and three normalized global datasets of experimental data obtained from the literature (dashed-contour grey-filled boxes) $\{\{R; ACV\}, \{R; AHP\}, \{R; S_{MN}\}\}$ and $\{\{I_{th}; R\}, \{I_{th}; AHP\}, \{I_{th}; ACV\}\}$. The $\{R; ACV\}$ and $\{R; AHP\}$ datasets were first transformed ($\otimes$ symbol) into two intermediary $\{R; S_{MN}\}$ datasets (dotted-contour boxes) by converting the ACV and AHP values to equivalent S_{MN} values with two 'inverse' $S_{MN} = f_{ACV}(ACV)$ and $S_{MN} = f_{AHP}(AHP)$ power relationships (oval boxes with triple dots), which had been previously obtained from two unshown steps that had yielded the final $\{ACV; S_{MN}\}$ and $\{AHP; S_{MN}\}$ datasets. The two intermediary $\{R; S_{MN}\}$ datasets were merged with the remaining global $\{R; S_{MN}\}$ dataset to yield the final $\{R; S_{MN}\}$ dataset, to which a power relationship of the form $R = k \cdot S_{MN}^c$ was fitted. If $r^2 > 0.3$ and p<0.01, an 'inverse' power relationship $S_{MN} = f_R(R)$ (oval box) was further fitted to this final dataset. In a similar approach, the three normalized global datasets $\{I_{th}; R\}, \{I_{th}; AHP\}$, and $\{I_{th}; ACV\}$ were transformed with the three 'inverse' relationships into intermediary $\{I_{th}; S_{MN}\}$ datasets, which were merged to yield the final $\{I_{th}; S_{MN}\}$ dataset. An 'inverse' $S_{MN} = f_{I_{th}}(I_{th})$ power relationship was further derived to be used in the creation of the final $\{C; S_{MN}\}$ and $\{\tau; S_{MN}\}$ datasets in the next taken steps.

Normalized mathematical relationships between electrophysiological properties

When a final relationship with S_{MN} was obtained for two MN properties A and B by the procedure described above, that is, $A = k_{cA} \cdot S_{MN}^{c_A}$ and $B = k_{cB} \cdot S_{MN}^{c_B}$, one of the expressions was mathematically inverted and a third empirical relationship was derived for the property pair $\{A; B\}$:

$$A = \frac{k_{cA}}{(k_{cB})^{\frac{c_A}{c_B}}} \cdot (B)^{\frac{c_A}{c_B}} = k_e \cdot B^e$$

This procedure was applied to all possible $\{A; B\}$ pairs in **Table 1**.

Validation of the normalized relationships

The normalized relationships were validated using a standard fivefold cross-validation procedure (**Chollet, 2021**). The data in each $\{A; B\}$ global normalized dataset was initially randomized and therefore made independent from the studies constituting it. Each shuffled global dataset was then split into five non-overlapping complementary partitions, each containing 20% of the data. Four partitions including 80% of the data were taken to constitute a training set from which the normalized

relationships were built as described previously. The latter equations were validated against the last data partition, which includes the remaining 20% of the data and which is called test set in the following. To perform this validation, the final size-related relationships $A = k_c \cdot S_{MN}^c$ and relationships between electrophysiological properties $A = k_e \cdot B^e$ obtained with the training set were applied to the S_{MN} or B data in each test set, yielding predicted values A. It was then assessed to what extent the mathematical relationships predicted the test data A by calculating the normalized maximum error (nME), the normalized root mean squared error ($nRMSE$) and the coefficient of determination r_{pred}^2 between predicted and control values of A in each test set. This process was repeated for a total of five times by permutating the five data partitions and creating five different pairs of one training set and one test set. The nME, $nRMSE$, and r_{pred}^2 values were finally averaged across the five permutations. For each global dataset, the average r_{pred}^2 was compared to the r_{exp}^2 obtained from the power trendlines least-squared fitted to the control data in the log–log space. Once validated with this fivefold cross-validation method, the final normalized size-dependent relationships $A = k_c \cdot S_{MN}^c$ and relationships between electrophysiological properties $A = k_e \cdot B^e$ were computed for the complete global datasets.

Scaling of the normalized relationships

The $A = k_c \cdot S_{MN}^c$ and $A = k_e \cdot B^e$ normalized relationships were finally scaled to typical cat property values in three steps. First, it was assessed from the literature the fold range over which each MN property was to vary. S_{MN} varied over a q_S^E-fold range, taken as the average across cat studies of the ratios of minimum and maximum values measured for S_{MN}:

$$q_S^E = \frac{1}{N_{studies}} \sum_{i=1}^{N_{studies}} \left[\frac{(S_{MNi})_{max}}{(S_{MNi})_{min}} \right]$$

An experimental ratio q_A^E was similarly obtained for each electrophysiological property A. As $A = k_c \cdot S_{MN}^c$, any electrophysiological property A could theoretically vary over a $q_A^T = \left(q_S^E \right)^{|c|}$-fold range, which was compared to q_A^E for consistency in the results. Then, a theoretical range $[A_{min}; A_{max}]$ of values were derived for each electrophysiological property A. Defining A_{min}^E and A_{max}^E as the respective average of the minimum and maximum A-values across studies, it was enforced $\frac{A_{max}}{A_{min}} = q_A^T$ and $\frac{A_{min} + A_{max}}{2} = \frac{A_{min}^E + A_{max}^E}{2}$ so that the $[A_{min}; A_{max}]$ theoretical ranges were consistent with the normalized size-dependent relationships while best reproducing the experimental data from cat literature. A theoretical range for $S_{MN}[(S_{MN})_{min}; (S_{MN})_{max}]$ was similarly built over the q_S^E-fold range previously derived. Finally, the intercept k_c in the size-dependent relationships $A = k_c \cdot S_{MN}^c$ was scaled as

$$\begin{cases} k_c = \frac{A_{min}}{(S_{MN})_{min}^c} & ; \ if \ c > 0 \\ k_c = \frac{A_{max}}{(S_{MN})_{min}^c} & ; \ if \ c < 0 \end{cases}$$

A similar approach was used to mathematically derive the intercept k_e and scale the relationships $A = k_e \cdot B^e$ between electrophysiological properties.

Extrapolation to rats and mice

It was finally assessed whether the $A = k_c \cdot S_{MN}^c$ and $A = k_e \cdot B^e$ scaled relationships derived from cat data accurately predicted rat and mouse quantities reported in other experimental studies. These mathematical relationships were applied to the S_{MN} or B data in each $\{A; B\}$ global dataset of absolute values obtained for rats and mice independently. The accuracy in predicting the quantity A was assessed for each available dataset with the same three validation metrics used to validate the normalized power trend lines: the normalized maximum error (nME), the normalized root-mean-square error ($nRMSE$) and the coefficient of determination r^2 between predicted and experimental values of A.

Definitions of MN size S_{MN} and mU size S_{mU}

MN size S_{MN}

The selected studies that performed both electrophysiological and morphometric measurements on the same MNs dominantly measured the MN soma diameter D_{soma} as an index of MN size. Therefore,

we chose $S_{MN} = D_{soma}$ in the described methodology. In the literature on spinal MNs in adult mammals, the size of an MN S_{MN} is also related to the measures of the somal cross-sectional area CSA_{soma} (**Gao et al., 2009**; **Friese et al., 2009**; **Deardorff et al., 2013**; **Mierzejewska-Krzyżowska et al., 2014**; **Dukkipati et al., 2018**), soma surface area S_{soma} (**Ulfhake and Kellerth, 1984**; **Brandenburg et al., 2020**), axonal diameter D_{axon} (**Cullheim, 1978**), individual dendrite diameter $D_{dendrite}$ (**Amendola and Durand, 2008**; **Carrascal et al., 2009**; **Mantilla et al., 2018**), individual dendritic surface area $S_{dendrite}$ (**Li et al., 2005**; **Obregón et al., 2009**; **Carrascal et al., 2009**; **Filipchuk and Durand, 2012**; **Kanjhan et al., 2015**), total dendritic surface area (**Ulfhake and Cullheim, 1988**; **Amendola and Durand, 2008**; **Brandenburg et al., 2020**), or total MN surface area S_{neuron} (**Burke et al., 1982**) defined as the summed soma and dendritic surface areas.

In the references (**Zwaagstra and Kernell, 1981**; **Ulfhake and Kellerth, 1981**), a linear correlation between D_{soma} and the average diameter of the stem dendrites $D_{dendrite_{mean}}$ has been reported ($r > 0.62$, population size in {40; 82} cells). Moreover, a linear or quasi-linear correlation has been found (**Cullheim et al., 1987**; **Ulfhake and Cullheim, 1988**; **Moschovakis et al., 1991**; **Prakash et al., 2000**; **Li et al., 2005**; **Obregón et al., 2009**; **Mantilla et al., 2018**) between the stem dendrite diameter $D_{dendrite}$ and the membrane surface area of the corresponding dendritic tree $S_{dendrite}$ ($r > 0.78$, population size in $[33; 342]$ dendrites). Therefore, from these studies, we can assume an approximate linear correlation between D_{soma} and the average dendritic surface area $S_{dendrite_{mean}}$. Moreover, the number of dendritic trees $N_{dendrites}$ per cell increases with increasing soma surface S_{soma} (**Brandenburg et al., 2018**), and a linear correlation between D_{soma} or $S_{dendrites}$ with $N_{dendrites}$ has been observed (**Zwaagstra and Kernell, 1981**; **Ulfhake and Cullheim, 1988**; **Amendola and Durand, 2008**) ($r > 0.40$, population size in {14; 32; 87} cells). It was therefore assumed that D_{soma} and total dendritic surface area $S_{dendrite}^{tot}$ are linearly correlated. This assumption/approximation is consistent other conclusions of a linear correlations between D_{soma} and $S_{dendrite}^{tot}$ (**Amendola and Durand, 2008**; **Brandenburg et al., 2020**). Then, according to typical values of D_{soma}, S_{soma}, and $S_{dendrites}^{tot}$ obtained from the studies previously cited, yielding $S_{dendrites}^{tot} \gg S_{soma}$, it was also assumed $S_{dendrites}^{tot} \approx S_{neuron}$. It is thus concluded that D_{soma} is linearly related to total neuron membrane area S_{neuron}, consistently with results by **Burke et al., 1982** ($r = 0.61$, 57 cells).

For the above reasons and assumptions, the mathematical relationships $A = k_c \cdot S_{MN}^c$ derived previously, with $S_{MN} = D_{soma}$, were extrapolated with a gain to relationships between A and $S_{MN} = S_{neuron}$, notably permitting the definition of surface specific resistance R_m and capacitance C_m. Following the same method as described above, theoretical ranges $[(S_{neuron})_{min}; (S_{neuron})_{max}]$ were derived from additional morphometric studies on adult cat spinal alpha-MNs. The new relationships were extrapolated as $A = k_c \cdot D_{soma}^c = \frac{(S_{neuron})_{min}}{(D_{neuron})_{min}} \cdot S_{neuron}^c$.

It must however be highlighted that the conclusion of a linear correlation between D_{soma} and S_{neuron}, while plausible, is crude. Morphometric measurements of individual MNs are indeed difficult and suffer many limitations. MN staining, slice preparations, and MN reconstruction and identification are complex experimental procedures requiring a large amount of work; the results from most of the cited studies thus rely on relatively small pools of investigated MNs. Most cited studies did not account for tissue shrinkage after dehydration, while some may have failed to assess the full dendritic trees from MN staining techniques (**Brandenburg et al., 2020**), thus underestimating dendritic membrane measurements. Moreover, before automated tools for image segmentation, landmark mapping, and surface tracking (**Amendola and Durand, 2008**; **Obregón et al., 2009**; **Mierzejewska-Krzyżowska et al., 2014**) were available, morphometric measurements were performed from the manual reproduction of the cell outline under microscope, yielding important operator errors reported to be of the order of ~0.5 μm, that is, $\sim 20\%$ stem diameter. In these studies, morphological quantities were besides obtained from geometrical approximations of the 2D MN shape, such as modelling the individual dendritic branches as one (**Cullheim et al., 1987**) or more (**Prakash et al., 2000**) equivalent cylinders for the derivation of $S_{dendrite}$. Morphometric measurement approaches also varied between studies; for example, oval or circle shapes were best fitted by sight onto the soma outline and equivalent D_{soma} quantities were derived either as the mean of measured maximum and minimum oval diameters or as the equivalent diameter of the fitted circle. In these studies, CSA_{soma} and S_{soma} were therefore derived by classical equations of circle and spheric surface areas, which contradicts the results by **Mierzejewska-Krzyżowska et al., 2014** obtained from surface segmentation of a linear relationship between D_{soma} and CSA_{soma} ($r = 0.94$, 527 MNs). Finally, no correlation between soma size

Table 2. Measurable indices of motoneuron (MN) and muscle unit (mU) sizes in mammals. S_{MN} and S_{mU} are conceptual parameters which are adequately described by the measurable and linearly inter-related quantities reported in this table.

MN size (S_{MN})	mU size (S_{mU})
S_{neuron}	F^{tet}
D_{soma}	IR
	CSA^{mean}
	CSA^{tot}

and $N_{dendrites}$ was found (**Ulfhake and Kellerth, 1981**; **Cullheim et al., 1987**). Therefore, the linear correlation between D_{soma} and S_{neuron} is plausible but crude and requires awareness of several important experimental limitations and inaccuracies. Conclusions and predictions involving S_{neuron} should be treated with care in this study as these morphometric measurements lack the precision of the measures performed for the electrophysiological properties listed in **Table 1**.

Muscle unit size S_{mU}

To enable future comparisons between MN and mU properties, we here assess potential indices of the mU size S_{mU} suggested in the literature. The size of an mU (S_{mU}) can be defined as the sum CSA^{tot} of the CSAs of the innervated fibres composing the mU. CSA^{tot} depends on the mU innervation ratio (IR) and on the mean CSA (CSA^{mean}) of the innervated fibres: $S_{mU} = CSA^{tot} = IR \cdot CSA^{mean}$. CSA^{tot} was measured in a few studies on cat and rat muscles, either indirectly by histochemical fibre profiling (**Burke and Tsairis, 1973**; **Dum and Kennedy, 1980**; **Burke, 1981**), or directly by glycogen depletion, periodic acid Schiff (PAS) staining and fibre counting (**Burke et al., 1982**; **Rafuse et al., 1997**). The mU tetanic force F^{tet} is however more commonly measured in animals. As the fibre mean specific force σ is considered constant among the mUs of one muscle in animals (**Lucas et al., 1987**; **Enoka, 1995**), the popular equation $F^{tet} = \sigma \cdot IR \cdot CSA^{mean}$ (**Burke, 1981**; **Enoka, 1995**) returns a linear correlation between F^{tet} and $IR \cdot CSA^{mean} = S_{mU}$ in mammals. Experimental results (**Burke and Tsairis, 1973**; **Bodine et al., 1987**; **Chamberlain and Lewis, 1989**; **Kanda and Hashizume, 1992**; **Rafuse et al., 1997**; **Hegedus et al., 2007**) further show a linear correlation between F^{tet} and IR and between F^{tet} and CSA^{mean}. Consequently, F^{tet}, IR, and CSA^{mean} are measurable, consistent, and linearly related measures of S_{mU} in animals, as summarized in **Table 2**.

Relationships between MN and mU properties

To assess whether the size-dependent relationships $A = k_c \cdot S_{MN}^c$ derived in this study were in accordance with Henneman's size principle of motor unit recruitment, we identified a set of experimental studies that concurrently measured an MN property B_{MN} (**Table 1**) and an mU property A_{mU} for the same MU. The normalized global datasets obtained for the pairs $\{A_{mU}; B_{MN}\}$ were fitted with power trendlines, as previously described for MN properties, yielding $A_{mU} = k \cdot B_{MN}^b$ relationships. Using both the definition of S_{mU} (**Table 2**) and the $A = k_c \cdot S_{MN}^c$ relationships derived previously, the $A_{mU} = k \cdot B_{MN}^b$ relationships were then mathematically transformed into $S_{mU} = k \cdot S_{MN}^c$ relationships. If all c-values obtained from different $\{A_{mU}; B_{MN}\}$ pairs were of the same sign, it was concluded that mU and MN sizes were monotonically related. Considering the limited data available obtained from the literature, data obtained for MNs innervating different hindlimb muscles were merged. Also, cat, rat, and mouse studies were processed independently but the resulting c-values were compared without regards to the related species.

Results

We respectively identified 19, 6, and 4 studies respecting our desired criteria on cats, rats, and mice that reported processable experimental data for the morphometric and electrophysiological properties listed in **Table 1**. Additional publications including some from the past 10 years were identified but could not be included in this work as no processable data could be recovered. An additional 14 studies were found to perform concurrent MN and mU measurements on individual motor units. From the selected cat studies, the 17 pairs of MN properties and the 8 pairs of one MN and one mU property represented in the bubble diagram of **Figure 2A** were investigated.
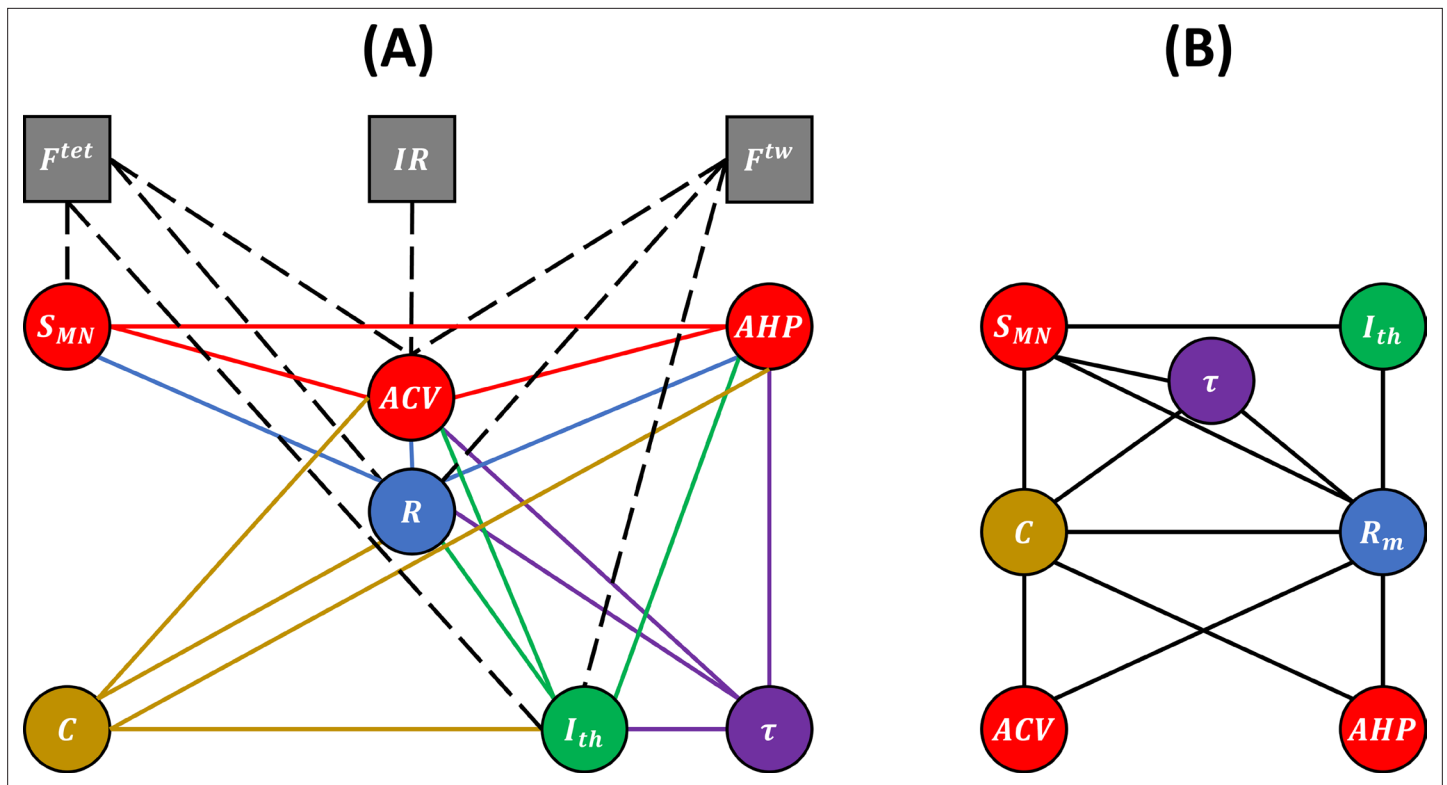
Figure 2. Experimental (**A**) and unknown (**B**) relations between motoneuron (MN) and muscle unit (mU) properties. (**A**) Bubble diagram representing the pairs of MN and/or mU properties that could be investigated in this study from the results provided by the 40 studies identified in our web search. MN and mU properties are represented by circle and square bubbles, respectively. Relationships between MN properties are represented by coloured connecting lines; the colours red, blue, green, yellow, and purple are consistent with the order ACV, AHP, R, I_{th}, C, τ in which the pairs were investigated (see **Table 3** for mathematical relationships). Relationships between one MN and one mU property are represented by black dashed lines. (**B**) Bubble diagram representing the mathematical relationships proposed in this study between pairs of MN properties for which no concurrent experimental data has been measured to date.

Relationships between MN properties

Global datasets and data variability

The experimental data retrieved from the selected studies for the 17 pairs of MN properties drawn in **Figure 2A** were merged into 17 normalized global datasets plotted in **Figure 3**. Eight global datasets ($\{ACV; S_{MN}\}$, $\{AHP; ACV\}$, $\{R; S_{MN}\}$, $\{R; ACV\}$, $\{R; AHP\}$, $\{I_{th}; R\}$, $\{I_{th}; ACV\}$, $\{\tau; R\}$) included the data from two or more experimental studies.

These studies reported in each global dataset similar normalized property distributions, as visually displayed in the frequency histograms in **Appendix 1—figure 1**. This was confirmed by the $mean_g \pm sd_g$ calculations described in 'Methods' of the four metrics range, mean, CoV, and $\frac{Me}{Md}$ displayed as error bars in **Appendix 1—figure 2**. Out of the 64 $mean_g$ +/- sd_g calculations (4 metrics for 16 property distributions of the 8 global datasets), 55 (86%) returned $sd_g < 10\%$ and $\frac{sd_g}{mean_g} < 0.15$. Otherwise, the distributions of only three, two, and four properties showed sensibly higher inter-study variability in the global datasets for the range, mean, and CoV metrics, respectively, however, still verifying $sd_g < 15\%$ and $\frac{sd_g}{mean_g} < 0.33$. Additional details are provided in Appendix 1. Then, as displayed in **Figure 3** and reported in **Table 3**, power trendlines and their 95% confidence interval were fitted to the global datasets. All 17 trendlines were statistically significant and adequately represented by a power model $A = k_a \cdot B^a$ (p-value<10⁻⁵ and $r^2 \in [0.34; 0.72]$ for 15 datasets; p-value<10⁻⁵ and $r^2 \in \{0.24; 0.17\}$ for the $\{C; AHP\}$ and $\{C; ACV\}$ datasets, respectively). As displayed in green dotted lines in **Figure 3**, the confidence interval remained narrow for all datasets with the value of power a varying less than 0.4, except for the $\{I_{th}; ACV\}$ dataset, suggesting a low inter-study variability in associating the distributions of two properties. As displayed in **Appendix 1—figure 3**, the selected studies however reported datasets of different sizes. Yet, out of the 35 experimental datasets constituting the 8 global datasets
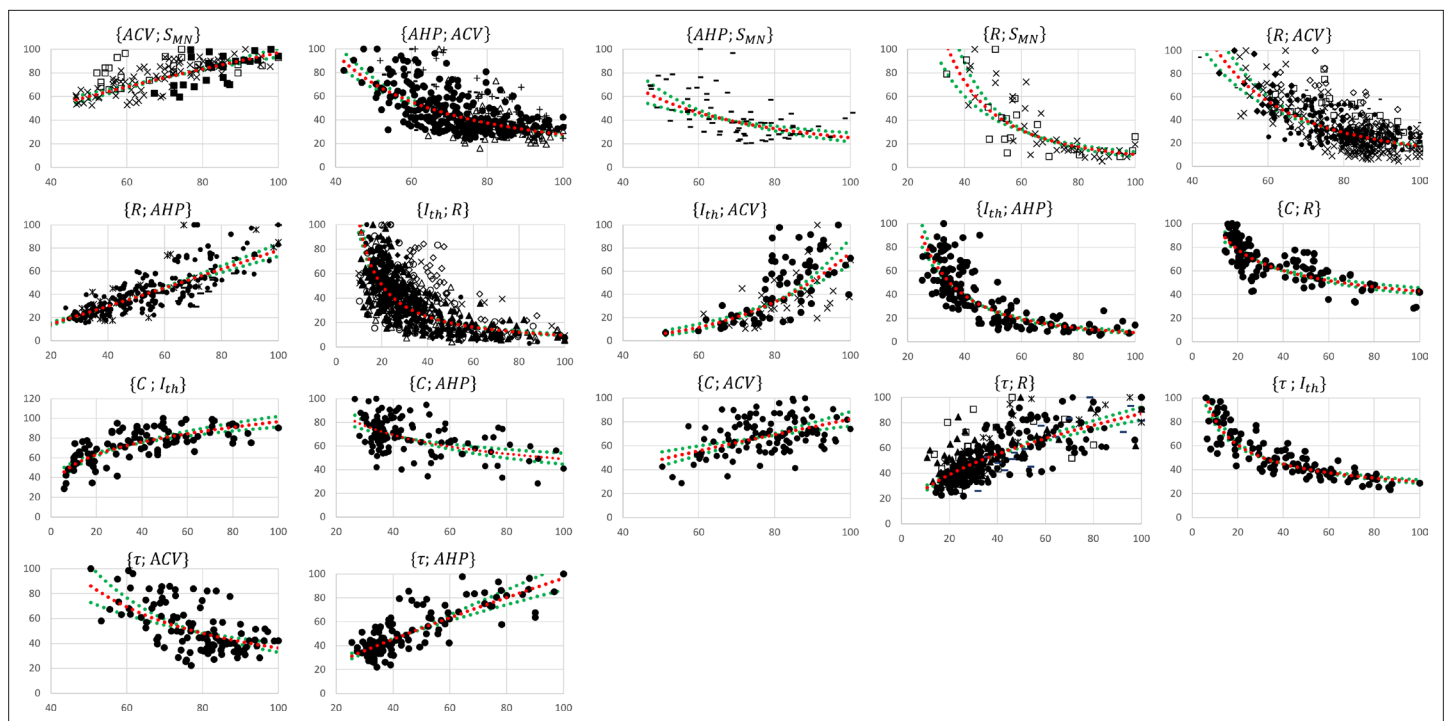
Figure 3. Normalized global datasets. These were obtained from the 19 studies reporting cat data that measured and investigated the 17 pairs of motoneuron (MN) properties reported in *Figure 2A*. For each $\{A; B\}$ pair, the property A is read on the y-axis and B on the x-axis. For information, power trendlines $A = k \cdot B^a$ (red dotted curves) are fitted to the data of each dataset and reported in *Table 3*. The 95% confidence interval of the regression is also displayed for each dataset (green dotted lines). The studies are identified with the following symbols: • (*Gustafsson, 1979*; *Gustafsson and Pinter, 1984a*; *Gustafsson and Pinter, 1984b*), ○ (*Munson et al., 1986*), ▲ (*Zengel et al., 1985*), △ (*Foehring et al., 1987*), ■ (*Cullheim, 1978*), □ (*Burke, 1968*; *Burke and ten Bruggencate, 1971*; *Burke et al., 1982*), ◆(*Krawitz et al., 2001*), ◇ (*Fleshman et al., 1981*), + (*Eccles et al., 1958b*), X (*Kernell, 1966*; *Kernell and Zwaagstra, 1981*; *Kernell and Monster, 1981*), - (*Zwaagstra and Kernell, 1980*), — (*Sasaki, 1991*), ✶ (*Pinter and Vanden Noven, 1989*). The axes are given in % of the maximum retrieved values in the studies consistently with 'Methods' section.

The online version of this article includes the following source data for figure 3:

Source data 1. All the cat datasets presented in *Figure 3*.

identified previously, only 1 and 7 experimental datasets were identified to respectively constitute more than 50% and less than 10% of the global dataset they were included in. Therefore, despite a general imbalance towards the over-appearance of the work from *Gustafsson and Pinter, 1984a*; *Gustafsson and Pinter, 1984b* and a tendency towards overlooking some small datasets (*Kernell, 1966*; *Burke and ten Bruggencate, 1971*; *Sasaki, 1991*), the remaining studies all played a significant role in the procedure to constitute the final datasets. Therefore, the inter-study data variability was globally low, and the data distributions reported in the experimental studies were confidently merged into the global datasets plotted in *Figure 3*. It is worth noting that three research groups provided 40, 27, and 15% of the 2717 data points describing the S_{MN}, ACV, AHP, R, I_{th}, and τ property distributions in this study, while the C-related data was provided by one only research group, leading to potential group-specific methodological bias.

The merged property distributions obtained in the 17 global datasets showed low variability between global datasets, as displayed in *Appendix 1—figure 4*. Indeed, $sd_G < 10\%$ and $\frac{sd_G}{mean_G} < 0.15$ were obtained for all four metrics for all the investigated properties across the global datasets they appeared in. Therefore, the property distributions were similar enough between global datasets to apply the process displayed in *Figure 1* and derive the final size-dependent datasets.

Size-dependent normalized relationships

The 17 normalized global datasets were processed according to the procedure described in *Figure 1* to derive normalized mathematical relationships between the electrophysiological properties listed in *Table 1* and MN size S_{MN}. First, the normalized size-dependent relationship $ACV = 4.0 \cdot S_{MN}^{0.7}$, reported

Table 3. Fitted experimental data of pairs of motoneuron (MN) properties and subsequent normalized final size-related relationships. For information, the r^2, p-value, and the equation $A = k_a \cdot B^a$ are reported for each fitted global dataset. The normalized MN-size dependent relationships $A = k_c \cdot S_{MN}^c$ are mathematically derived from the transformation of the global datasets and from the power trendline fitting of the final datasets (N data points) as described in 'Methods'. The minimum and maximum values of k_a, k_c, a, and c defining the 95% confidence interval of the regression are also reported in parenthesis for each global and final dataset. The r^2 values reported in this table are consistent with the r^2 values obtained when directly fitting the normalized experimental datasets with power regressions (see **Appendix 1—table 1**).

| MN property	Relationship	$A = k_a \cdot B^a$ (normalized global datasets)				Reference studies	$A = k_c \cdot S_{MN}^c$ (final MN-size dependent datasets)				
A		k_a	a	r^2	p-value		k_c	c	r^2	p-value	N points
ACV	$ACV = k_a \cdot S_{MN}^a$	4.0 (2.5; 6.4)	0.7 (0.6; 0.8)	0.58	$<10^{-5}$	Cullheim, 1978; Kernell and Zwaagstra, 1981; Burke et al., 1982	4.0 (2.5; 6.4)	0.7 (0.6; 0.8)	0.58	$<10^{-5}$	109
AHP	$AHP = k_a \cdot S_{MN}^a$	$6.1 \cdot 10^3$ ($1.2 \cdot 10^3$; $3.2 \cdot 10^4$)	−1.2 (−1.6; −0.8)	0.34	$<10^{-5}$	Zwaagstra and Kernell, 1980	$2.5 \cdot 10^4$ ($1.2 \cdot 10^4$; $5.0 \cdot 10^4$)	−1.5 (−1.7; −1.3)	0.41	$<10^{-5}$	492
	$AHP = k_a \cdot ACV^a$	$1.5 \cdot 10^4$ ($7.4 \cdot 10^3$; $2.9 \cdot 10^4$)	−1.4 (−1.5; −1.2)	0.41	$<10^{-5}$	Eccles et al., 1958a; Zwaagstra and Kernell, 1980; Gustafsson and Pinter, 1984b; Foehring et al., 1987					
R	$R = k_a \cdot S_{MN}^a$	$1.5 \cdot 10^5$ ($2.7 \cdot 10^4$; $7.9 \cdot 10^5$)	−2.1 (−2.5; −1.7)	0.61	$<10^{-5}$	Kernell and Zwaagstra, 1981; Burke et al., 1982	$9.6 \cdot 10^5$ ($4.1 \cdot 10^5$; $2.3 \cdot 10^6$)	−2.4 (−2.6; −2.2)	0.37	$<10^{-5}$	745
	$R = k_a \cdot ACV^a$	$6.3 \cdot 10^5$ ($1.9 \cdot 10^5$; $2.1 \cdot 10^6$)	−2.3 (−2.6; −2.0)	0.38	$<10^{-5}$	Kernell, 1966; Burke, 1968; Barrett and Crill, 1974; Kernell and Zwaagstra, 1981; Fleshman et al., 1981; Gustafsson and Pinter, 1984b; Sasaki, 1991					
	$R = k_a \cdot AHP^a$	$6.2 \cdot 10^{-1}$ ($4.1 \cdot 10^{-1}$; $9.2 \cdot 10^{-1}$)	1.1 (0.9; 1.2)	0.65	$<10^{-5}$	Gustafsson, 1979; Gustafsson and Pinter, 1984b; Foehring et al., 1987; Pinter and Vanden Noven, 1989; Sasaki, 1991					
I_{th}	$I_{th} = k_a \cdot R^a$	$1.1 \cdot 10^3$ ($0.8 \cdot 10^3$; $1.3 \cdot 10^3$)	−1.0 (−1.1; −0.9)	0.37	$<10^{-5}$	Kernell, 1966; Fleshman et al., 1981; Gustafsson and Pinter, 1984a; Zengel et al., 1985; Munson et al., 1986; Foehring et al., 1987; Krawitz et al., 2001	$9.0 \cdot 10^{-4}$ ($4.7 \cdot 10^{-4}$; $1.7 \cdot 10^{-3}$)	2.5 (2.4; 2.7)	0.37	$<10^{-5}$	722
	$I_{th} = k_a \cdot ACV^a$	$3.2 \cdot 10^{-6}$ ($1.3 \cdot 10^{-7}$; $8.2 \cdot 10^{-5}$)	3.7 (3.0; 4.4)	0.37	$<10^{-5}$	Kernell and Monster, 1981; Gustafsson and Pinter, 1984a					
	$I_{th} = k_a \cdot AHP^a$	$2.5 \cdot 10^4$ ($1.3 \cdot 10^4$; $4.8 \cdot 10^4$)	−1.7 (−1.9; −1.6)	0.60	$<10^{-5}$	Gustafsson and Pinter, 1984a					
C	$C = k_a \cdot R^a$	$2.4 \cdot 10^2$ ($2.0 \cdot 10^2$; $3.9 \cdot 10^2$)	−0.4 (−0.4; −0.3)	0.57	$<10^{-5}$	Gustafsson and Pinter, 1984b	1.2 (0.7; 2.0)	1.0 (0.9; 1.2)	0.28	$<10^{-5}$	444
	$C = k_a \cdot I_{th}^a$	$2.9 \cdot 10^1$ ($2.4 \cdot 10^1$; $3.5 \cdot 10^1$)	0.3 (0.2; 0.3)	0.51	$<10^{-5}$	Gustafsson and Pinter, 1984a					
	$C = k_a \cdot AHP^a$	$2.8 \cdot 10^2$ ($1.8 \cdot 10^2$; $4.4 \cdot 10^2$)	−0.4 (−0.5; −0.3)	0.24	$<10^{-5}$	Gustafsson and Pinter, 1984b					
	$C = k_a \cdot ACV^a$	2.5 (0.7; 8.4)	0.8 (0.5; 1.0)	0.17	$<10^{-5}$	Gustafsson and Pinter, 1984b					
τ	$\tau = k_a \cdot R^a$	8.7 (7.2; 10.6)	0.5 (0.4; 0.6)	0.52	$<10^{-5}$	Burke and ten Bruggencate, 1971; Barrett and Crill, 1974; Gustafsson, 1979; Gustafsson and Pinter, 1984b; Zengel et al., 1985; Pinter and Vanden Noven, 1989; Sasaki, 1991	$2.6 \cdot 10^4$ ($1.5 \cdot 10^4$; $4.5 \cdot 10^4$)	−1.5 (−1.6; −1.4)	0.46	$<10^{-5}$	649
	$\tau = k_a \cdot AHP^a$	2.2 (1.3; 3.5)	0.8 (0.7; 1.0)	0.63	$<10^{-5}$	Gustafsson and Pinter, 1984b					
	$\tau = k_a \cdot I_{th}^a$	$2.3 \cdot 10^2$ ($1.9 \cdot 10^2$; $2.7 \cdot 10^2$)	−0.4 (−0.5; −0.3)	0.72	$<10^{-5}$	Gustafsson and Pinter, 1984a					
	$\tau = k_a \cdot ACV^a$	$1.2 \cdot 10^4$ ($2.2 \cdot 10^3$; $6.6 \cdot 10^4$)	−1.3 (−1.7; −0.9)	0.30	$<10^{-5}$	Gustafsson and Pinter, 1984b					
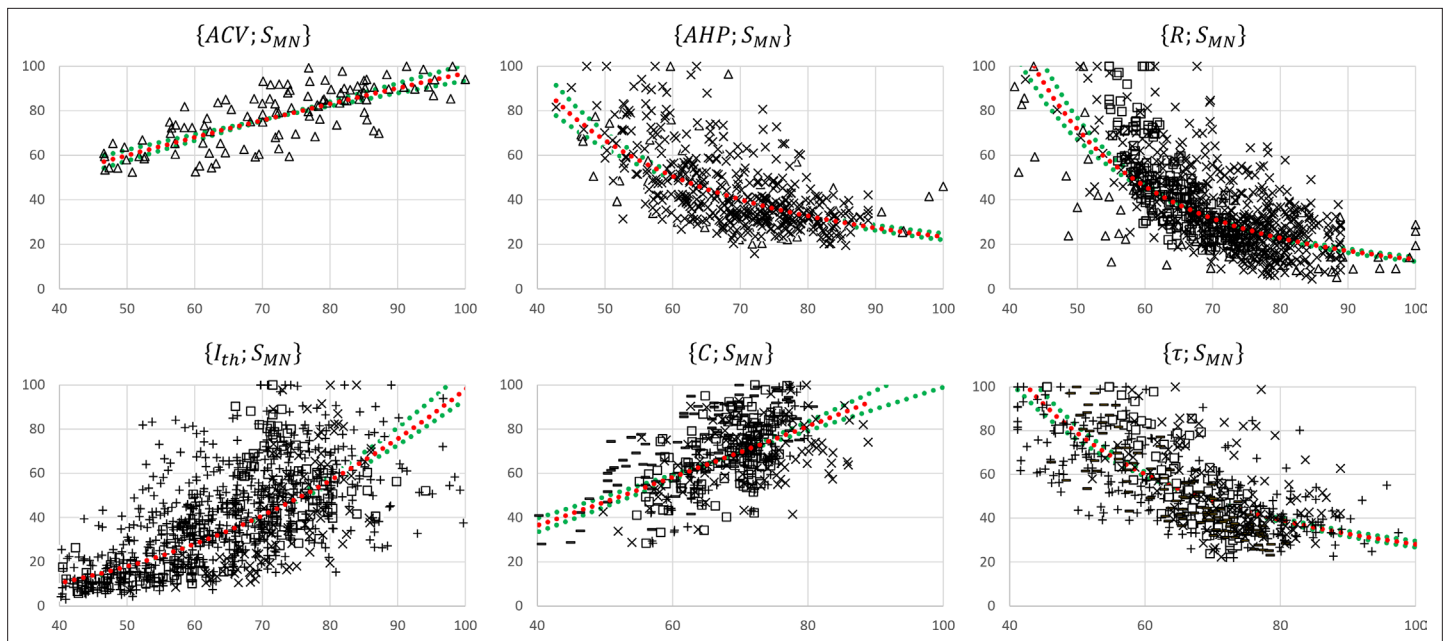
Figure 4. Normalized motoneuron (MN) size-related final datasets. These were obtained from the 19 studies reporting cat data that concurrently measured at least two of the morphometric and electrophysiological properties listed in **Table 1**. For each $\{A; S_{MN}\}$ pair, the property A is read on the y-axis and S_{MN} on the x-axis. The power trendlines $A = k_c \cdot S_{MN}^c$ (red dotted curves) are fitted to each dataset and are reported in **Table 3**. The 95% confidence interval of the regression is also displayed for each dataset (green dotted lines). For each $\{A; S_{MN}\}$ plot, the constitutive sub-datasets $\{A; S_{MN}\}$ that were obtained from different global $\{A; B\}$ datasets are specified with the following symbols identifying the property B: $S_{MN} \leftrightarrow \triangle$, $ACV \leftrightarrow \times$, $AHP \leftrightarrow \square$, $R \leftrightarrow +$, and $I_{th} \leftrightarrow -$.

in **Table 3**, was derived from the trendline fitting of the normalized $\{ACV; S_{MN}\}$ global dataset, which was obtained from three studies (**Cullheim, 1978**; **Kernell and Zwaagstra, 1981**; **Burke et al., 1982**) and is represented in the upper-left panel in **Figure 3**. This resulted in a statistically significant relationship ($r^2 = 0.58$, p-value<10⁻⁵). A statistically significant ($r^2 = 0.59$, p-value<10⁻⁵) inverse relationship $S_{MN} = k_d \cdot ACV^d$ was also fitted to this dataset. Then, the $\{AHP; ACV\}$ dataset, represented in the second panel upper row in **Figure 3** and obtained from four studies (**Eccles et al., 1958a**; **Zwaagstra and Kernell, 1980**; **Gustafsson and Pinter, 1984b**; **Foehring et al., 1987**), was transformed into a new $\{AHP; S_{MN}\}_1$ dataset by applying the priory-derived $S_{MN} = k_d \cdot ACV^d$ relationship to the list of ACV values. This transformed $\{AHP; S_{MN}\}_1$ dataset was then merged with the $\{AHP; S_{MN}\}_2$ dataset (third panel upper row in **Figure 2**) obtained from **Zwaagstra and Kernell, 1980**, yielding the final $\{AHP; S_{MN}\}_f$ dataset of $N = 492$ data points shown in **Figure 4**, second panel. A statistically significant ($r^2 = 0.58$, p-value<10⁻⁵) power trendline $AHP = 2.5 \cdot 10^4 \cdot S_{MN}^{-1.5}$ was fitted to the $\{AHP; S_{MN}\}_f$ dataset and is reported in **Table 3**. As before, a statistically significant ($r^2 = 0.38$, p-value<10⁻⁵) inverse relationship $S_{MN} = k_d \cdot AHP^d$ was also fitted to this dataset for future use. A similar procedure was applied to derive the normalized final relationships between $\{R, I_{th}, C, \tau\}$ and S_{MN} reported in the last column of **Table 3**. A statistically significant (p-value<10⁻⁵) correlation was obtained between each electrophysiological property $\{ACV, AHP, R, I_{th}, C, \tau\}$ and S_{MN} as reported in **Table 3**. With $r^2 \in [0.28; 0.58]$, it was obtained that $\{I_{th}, C, ACV\}$ and $\{R, AHP, \tau\}$ respectively increased and decreased with increasing MN sizes S_{MN}, with slopes reported in **Table 3** and plotted in **Figure 5**.

Normalized mathematical relationships between electrophysiological properties

The final size-dependent relationships reported in **Table 3** were mathematically combined to yield normalized relationships between all electrophysiological properties listed in **Table 1**. As an example, $I_{th} = 9.4 \cdot 10^{-4} \cdot S_{MN}^{2.5}$ and $R = 9.6 \cdot 10^5 \cdot S_{MN}^{-2.4}$ were obtained in **Table 3**. When mathematically combined (with the latter mathematically inverted as $S_{MN} = 2.9 \cdot 10^2 \cdot R^{-0.4}$), these relationships yielded the normalized relationship between rheobase and input resistance $I_{th} = 1.5 \cdot 10^3 \cdot R^{-1}$. All
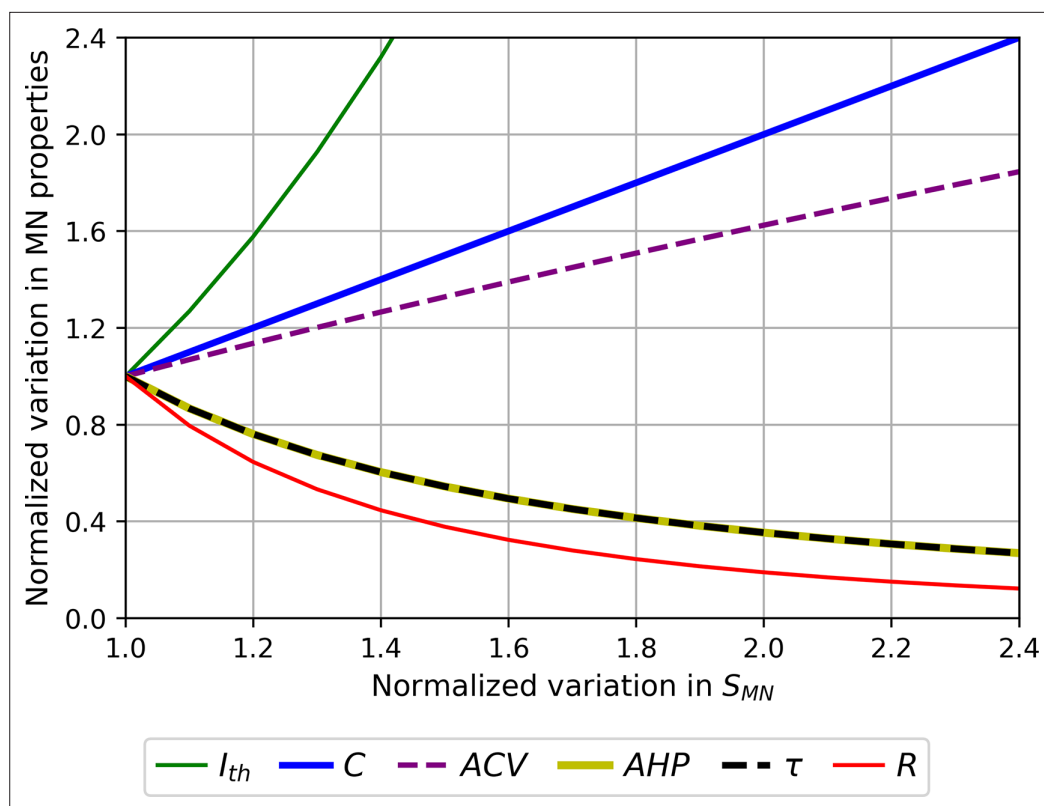
Figure 5. Normalized size-dependent behaviour of the motoneuron (MN) properties ACV, AHP, R, I_{th}, C, and τ. For displaying purposes, the MN properties are plotted in arbitrary units as power functions (intercept $k = 1$) of S_{MN}: $A = S_{MN}^c$ according to **Table 3**. The larger the MN size, the larger ACV, C, and I_{th} in the order of increasing slopes, and the lower AHP, τ and R in the order of increasing slopes.

normalized relationships between MN electrophysiological properties hence obtained are provided in **Appendix 1—table 2**.

Validation of the normalized relationships

The normalized relationships reported in **Appendix 1—table 2** were obtained from the complete global datasets represented in **Figure 3**. A fivefold cross-validation of these relationships was performed, as described in 'Methods', and assessed with calculations of the nME, $nRMSE$, and r_{pred}^2 validation metrics averaged across the five permutations. As displayed in **Figure 6**, the normalized relationships obtained from the 17 training datasets predicted, in average across the five permutations, the experimental data from the test datasets with average nME between 52 and 300%, $nRMSE$ between 13 and 24%, and coefficients of determination r_{pred}^2 between 0.20 and 0.74 and of the same order of magnitude as the experimental r_{exp}^2 values.

Scaling of the normalized relationships

The normalized relationships provided in **Appendix 1—table 2** were finally scaled to typical cat data obtained from the literature following the procedure described in 'Methods'. D_{soma} and S_{neuron} were found to vary in cats over an average $q_S^E = 2.4$-fold range according to a review of the morphometric studies reported in the two first lines of **Appendix 1—table 3**. q_S^E may however be underestimated for reasons discussed in Appendix 1. Then, the empirical q_A^E and theoretical q_A^T ratios, defined in 'Methods', were calculated for each MN electrophysiological property A and are reported in **Appendix 1—table 4**. For example, MN resistance R was found to vary over an average $q_R^E = 10.9$-fold range in an MN pool according to the literature, while the theoretical fold range $q_R^T = \left(q_S^E \right)^{|c_R|} = 2.4^{2.4} = 8.4$ was obtained from the $R = 9.6 \cdot 10^5 \cdot S_{MN}^{-2.4}$ normalized relationship previously derived when a 2.4-fold range is set
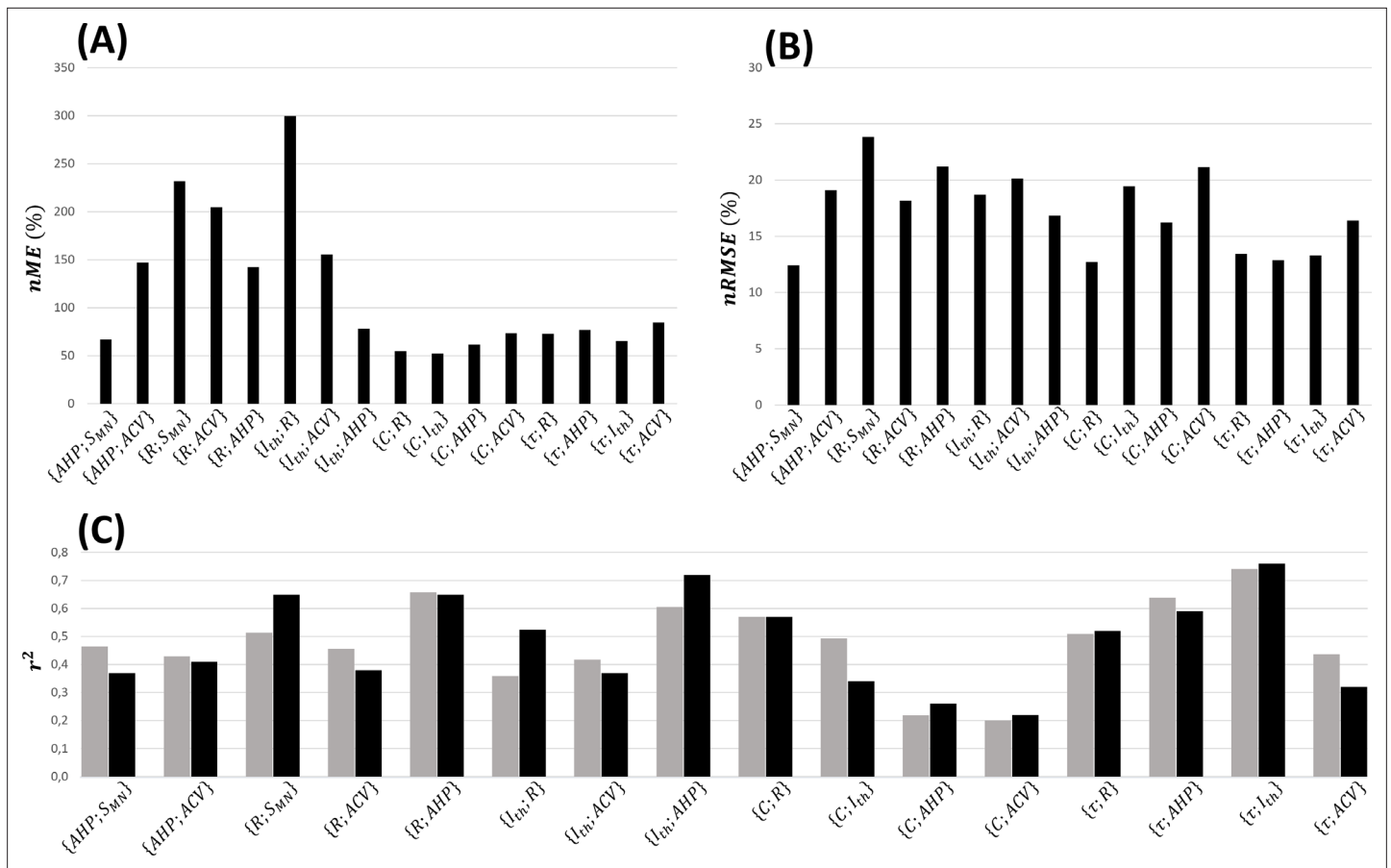
Figure 6. Fivefold cross-validation of the normalized mathematical relationships. Here are reported for each dataset the average values across the five permutations of (**A**) the normalized maximum error (*nME*), (**B**) the normalized root mean square error (*nRMSE*), and (**C**) coefficient of determination (r^2_{pred}, grey bars), which is compared with the coefficient of determination (r^2_{exp}, black bars) of the power trendline fitted to the log–log transformation of global experimental datasets directly.

for S_{MN}. As shown in **Appendix 1—table 4**, $\frac{q^E_A}{q^T_A} \in [0.8; 1.3]$ for the MN properties *ACV*, *AHP*, *C*, and τ, while the theoretical ranges for R and I_{th} span over a narrower domain than expected from experimental results ($q^T_R = 8.4 \ll 10.9 = q^E_R$ and $q^T_{I_{th}} = 9.1 \ll 16.3 = q^E_{I_{th}}$). This suggests that the range of variation of R and I_{th} is not entirely explained by the variation in MN size S_{MN}, and that MN excitability is not only determined by S_{MN}, as reviewed in **Powers and Binder, 2001**.

The normalized relationships were finally scaled using the theoretical ranges reported in the last column of **Appendix 1—table 4**. Taking the $\{I_{th}; R\}$ pair as example, as $I_{th} = 1.4 \cdot 10^3 \cdot R^{-1}$ (normalized relationship derived previously and provided in **Appendix 1—table 2**), $R \in [0.5; 4.0] \cdot 10^6 \Omega$ and $I_{th} \in [3.9; 35.0] \cdot 10^{-9} A$ (**Appendix 1—table 4**), it was directly obtained from 'Methods' that $I_{th} = \frac{2.7 \cdot 10^{-2}}{R}$ in SI base units. A similar approach yielded the final mathematical relationships reported in **Table 4** between all MN electrophysiological and morphometric properties *ACV*, *AHP*, *R*, I_{th}, *C*, τ, and S_{MN}. All constants and relationships are given in SI base units.

Predicting correlations between MN properties

With this approach, the correlations between MN properties that were never concurrently measured in the literature are predicted, as displayed in **Figure 2B**. Such unknown relationships were indirectly extracted from the combination of known relationships (**Table 3**) and typical ranges of values obtained from the literature for these properties. Due to the prior fivefold cross-validation of the relationships in **Table 4**, these findings are reliable as indirectly consistent with the literature data processed in this study.

Table 4. Mathematical empirical cat relationships between the motoneuron (MN) properties S_{neuron}, D_{soma}, R, R_m, C, τ, I_{th}, AHP, and ACV. Each column provides the relationships between one and the eight other MN properties. If one property is known, the complete MN profile can be reconstructed by using the pertinent line in this table. All constants and properties are provided in SI base units (metres, seconds, ohms, farads, and amperes). The relationships involving R_m were obtained from theoretical relationships involved in Rall's cable theory (see 'Discussion').

|	S_{neuron} [m²]	D_{soma} [m]	R [Ω]	R_m [Ω·m²]	C [F]	τ [s]	I_{th} [A]	AHP [s]	ACV [m·s⁻¹]
S_{neuron} [m²]		$D_{soma} = 1.8 \cdot 10^2 \cdot S_{neuron}$	$R = \frac{1.7 \cdot 10^{-10}}{S_{neuron}^{2.43}}$	$R_m = \frac{1.0 \cdot 10^{-10}}{S_{neuron}^{1.43}}$	$C = 1.3 \cdot 10^{-2} \cdot S_{neuron}$	$\tau = \frac{1.0 \cdot 10^{-12}}{S_{neuron}^{1.48}}$	$I_{th} = 3.8 \cdot 10^8 \cdot S_{neuron}^{2.52}$	$AHP = \frac{1.0 \cdot 10^{-11}}{S_{neuron}^{1.51}}$	$ACV = 3.0 \cdot 10^6 \cdot S_{neuron}^{0.69}$
D_{soma} [m]	$S_{neuron} = 5.5 \cdot 10^{-3} \cdot D_{soma}$		$R = \frac{5.1 \cdot 10^{-5}}{D_{soma}^{2.43}}$	$R_m = \frac{1.7 \cdot 10^{-7}}{D_{soma}^{1.43}}$	$C = 7.9 \cdot 10^{-5} \cdot D_{soma}$	$\tau = \frac{2.3 \cdot 10^{-9}}{D_{soma}^{1.48}}$	$I_{th} = 7.8 \cdot 10^2 \cdot D_{soma}^{2.52}$	$AHP = \frac{2.7 \cdot 10^{-8}}{D_{soma}^{1.51}}$	$ACV = 8.1 \cdot 10^4 \cdot D_{soma}^{0.69}$
R [Ω]	$S_{neuron} = \frac{9.5 \cdot 10^{-5}}{R^{0.41}}$	$D_{soma} = \frac{1.7 \cdot 10^{-2}}{R^{0.41}}$		$R_m = 5.7 \cdot 10^{-5} \cdot R^{0.59}$	$C = \frac{1.5 \cdot 10^{-6}}{R^{0.40}}$	$\tau = 9.6 \cdot 10^{-7} \cdot R^{0.61}$	$I_{th} = \frac{2.7 \cdot 10^{-2}}{R^{1.04}}$	$AHP = 1.3 \cdot 10^{-5} \cdot R^{0.62}$	$ACV = \frac{4.9 \cdot 10^3}{R^{0.29}}$
R_m [Ω·m²]	$S_{neuron} = \frac{1.5 \cdot 10^{-7}}{R_m^{0.70}}$	$D_{soma} = \frac{2.6 \cdot 10^{-5}}{R_m^{0.70}}$	$R = 6.8 \cdot 10^6 \cdot R_m^{1.70}$		$C = \frac{1.8 \cdot 10^{-9}}{R_m^{0.69}}$	$\tau = 1.4 \cdot 10^{-2} \cdot R_m^{1.04}$	$I_{th} = \frac{2.2 \cdot 10^{-9}}{R_m^{1.76}}$	$AHP = 2.2 \cdot 10^{-1} \cdot R_m^{1.06}$	$ACV = \frac{5.4 \cdot 10^1}{R_m^{0.48}}$
C [F]	$S_{neuron} = 1.2 \cdot 10^2 \cdot C$	$D_{soma} = 2.1 \cdot 10^4 \cdot C$	$R = \frac{1.5 \cdot 10^{-15}}{C^{2.48}}$	$R_m = \frac{1.7 \cdot 10^{-13}}{C^{1.46}}$		$\tau = \frac{8.6 \cdot 10^{-16}}{C^{1.51}}$	$I_{th} = 6.5 \cdot 10^{13} \cdot C^{2.57}$	$AHP = \frac{7.7 \cdot 10^{-15}}{C^{1.54}}$	$ACV = 8.2 \cdot 10^7 \cdot C^{0.71}$
τ [s]	$S_{neuron} = \frac{8.4 \cdot 10^{-9}}{\tau^{0.67}}$	$D_{soma} = \frac{1.5 \cdot 10^{-6}}{\tau^{0.67}}$	$R = 7.1 \cdot 10^9 \cdot \tau^{1.64}$	$R_m = 3.6 \cdot 10^1 \cdot \tau^{0.96}$	$C = \frac{1.6 \cdot 10^{-10}}{\tau^{0.66}}$		$I_{th} = \frac{1.6 \cdot 10^{-12}}{\tau^{1.70}}$	$AHP = 1.7 \cdot 10^1 \cdot \tau^{1.02}$	$ACV = \frac{7.5}{\tau^{0.47}}$
I_{th} [A]	$S_{neuron} = 4.0 \cdot 10^{-4} \cdot I_{th}^{0.40}$	$D_{soma} = 7.1 \cdot 10^{-2} \cdot I_{th}^{0.40}$	$R = \frac{3.1 \cdot 10^{-2}}{I_{th}^{0.96}}$	$R_m = \frac{7.4 \cdot 10^{-6}}{I_{th}^{0.57}}$	$C = 5.9 \cdot 10^{-6} \cdot I_{th}^{0.39}$	$\tau = \frac{1.2 \cdot 10^{-7}}{I_{th}^{0.59}}$		$AHP = \frac{1.5 \cdot 10^{-6}}{I_{th}^{0.60}}$	$ACV = 1.3 \cdot 10^4 \cdot I_{th}^{0.27}$
AHP [s]	$S_{neuron} = \frac{5.5 \cdot 10^{-8}}{AHP^{0.66}}$	$D_{soma} = \frac{9.8 \cdot 10^{-6}}{AHP^{0.66}}$	$R = 7.5 \cdot 10^7 \cdot AHP^{1.61}$	$R_m = 2.5 \cdot AHP^{0.95}$	$C = \frac{9.7 \cdot 10^{-10}}{AHP^{0.65}}$	$\tau = 6.2 \cdot 10^{-2} \cdot AHP^{0.98}$	$I_{th} = \frac{1.8 \cdot 10^{-10}}{AHP^{1.67}}$		$ACV = \frac{2.7 \cdot 10^1}{AHP^{0.46}}$
ACV [m·s⁻¹]	$S_{neuron} = 4.6 \cdot 10^{-10} \cdot ACV^{1.44}$	$D_{soma} = 8.3 \cdot 10^{-8} \cdot ACV^{1.44}$	$R = \frac{8.3 \cdot 10^{12}}{ACV^{3.50}}$	$R_m = \frac{2.3 \cdot 10^3}{ACV^{2.06}}$	$C = 9.0 \cdot 10^{-12} \cdot ACV^{1.41}$	$\tau = \frac{7.4 \cdot 10^1}{ACV^{2.14}}$	$I_{th} = 1.1 \cdot 10^{-15} \cdot ACV^{3.64}$	$AHP = \frac{1.4 \cdot 10^3}{ACV^{2.18}}$	
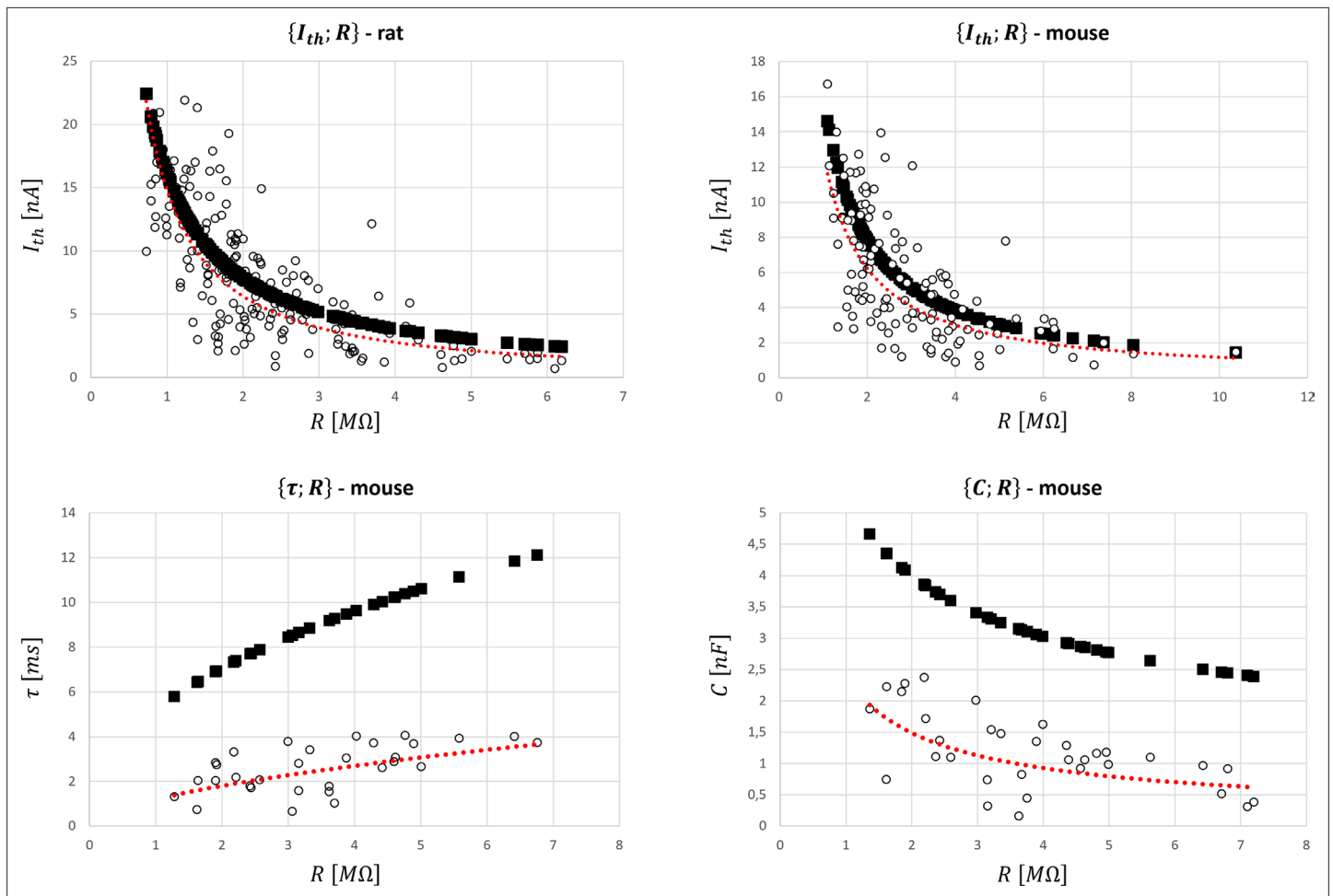
Figure 7. Global datasets for rat and mouse species and predictions of the motoneuron (MN) properties with the cat mathematical relationships (*Table 4*). They were obtained from the five studies reporting data on rats and the four studies presenting data on mice reported in *Appendix 1—table 5* that measured the $\{I_{th}; R\}$, $\{\tau; R\}$, and $\{C; R\}$ pairs of MN electrophysiological properties. I_{th}, R, τ, C are given in nA, MΩ, ms, and nF, respectively. The experimental data (O symbol) is fitted with a power trendline (red dotted curve) and compared to the predicted quantities obtained with the scaled cat relationships in *Table 4* (■ symbol).

The online version of this article includes the following source data for figure 7:

Source data 1. Datasets used in the rat plot.

Source data 2. Datasets used in the mouse plots.

Extrapolation to rats and mice

It was assessed whether the scaled relationships obtained from cat data and reported in *Table 4* could be successfully applied to rat and mouse data. A global $\{I_{th}; R\}$ dataset was obtained from five studies focussing on rats reported in *Appendix 1—table 5*, while four mice studies reported in *Appendix 1—table 5* provided processable data for the pairs $\{I_{th}; R\}$, $\{\tau; R\}$, and $\{C; R\}$. Only data from control groups of wild-type animals were considered while data on mutated, operated, or trained animals were disregarded. Because the information on the age distribution of the retrieved datasets is not available, data from adults rats and mice of unknown age were used, despite well-known age-related variations in the MN electrophysiological properties in these animals (*Highlander et al., 2020*; *Huh et al., 2021*). Like the cat data, low variability was observed between the R and I_{th} distributions reported by different studies in the rat and mouse $\{I_{th}; R\}$ datasets. *Figure 7* reports the global datasets for all four pairs of properties and the predictions obtained with the cat relationships reported in *Table 4*. As displayed in *Appendix 1—table 5*, r^2_{pred} and r^2_{exp} values were close for all four datasets, with a maximum 12.5% difference for $\{\tau; R\}$ in mice. *nRMSE* values remained low in both rat and mouse $\{I_{th}; R\}$ datasets, while being substantially higher in both $\{\tau; R\}$ and $\{C; R\}$ datasets in mice because of an inter-species-specific offset in the relationships.

Table 5. Fitted experimental data of pairs of one muscle unit (mU) and one motoneuron (MN) property and subsequent $S_{mU} \propto S_{MN}^c$ relationships.

The r^2, p-value, and the equation $A \propto B^c$ of the trendlines are reported for each pair of properties. In the last column, prior knowledge is used to derive relationships.

	$A = k \cdot B^c$ (fitted relationships)					(final relationships)
Species	Relationship	c	r^2	p-value	Reference studies	c
Rat	$IR = k \cdot ACV^c$	3.4	0.45	6.10^{-3}	*Kanda and Hashizume, 1992*	2.4
	$F^{tw} = k \cdot ACV^c$	9.4	0.43	$<10^{-5}$	*Knott et al., 1971*	6.6
	$F^{tet} = k \cdot ACV^c$	7.2	0.37	$<10^{-5}$	*Mcphedran et al., 1965; Wuerker et al., 1965; Appelberg and Emonet-Dénand, 1967; Proske and Waite, 1974; Bagust, 1974; Jami and Petit, 1975; Stephens and Stuart, 1975; Burke et al., 1982; Emonet-Dénand et al., 1988*	5.0
	$F^{tet} = k \cdot R^c$	-1.3	0.27	6.10^{-5}	*Dum and Kennedy, 1980*	3.2
Cat	$F^{tet} = k \cdot S_{MN}^c$	2.0	0.21	2.10^{-2}	*Burke et al., 1982*	2.0
	$F^{tw} = k \cdot R^c$	-2.1	0.42	$<10^{-5}$	*Manuel and Heckman, 2011; Martínez-Silva et al., 2018*	5.1
	$F^{tw} = k \cdot I_{th}^c$	1.3	0.64	2.10^{-4}	*Manuel and Heckman, 2011*	3.3
Mouse	$F^{tet} = k \cdot I_{th}^c$	1.0	0.80	6.10^{-2}	*Manuel and Heckman, 2011*	2.5
Mean ± sd						3.8 ± 1.5

The online version of this article includes the following source data for table 5:

Source data 1. Numerical data used to derive the relationships presented in *Table 5*.

Relationships between MN and mU properties

As shown in *Figure 2A*, eight pairs of one MN and one mU property were investigated in 14 studies in the literature in cats and rats. As remarked by *Heckman and Enoka, 2012* and *Manuel et al., 2019*, most recent studies were performed on mice, while most dated were dominantly performed on cats. One study on the rat gastrocnemius muscle (*Kanda and Hashizume, 1992*) indicated no correlation between IR and ACV. However, after removing from the dataset two outliers that fell outside 2 standard deviations of the mean IR data, a statistically significant correlation (p<0.05) between IR and ACV was successfully fitted with a power trendline ($r^2 = 0.43$). Eight studies, dominantly focussing on the cat soleus and medial gastrocnemius muscles, found a strong correlation between F^{tet} and ACV, while one study showed a significant correlation for the pair $\{F^{tet}; R\}$ in both the cat tibialis anterior and extensor digitorum longus muscles. One study (*Burke et al., 1982*) on the cat soleus, medial and lateral gastrocnemius muscles inferred a statistically significant correlation for $\{F^{tet}; S_{MN}\}$. In mice, both R and I_{th} were significantly related to muscle tetanic and twitch forces. As F^{tet}, F^{tw}, and IR are reliable indices of S_{mU} as discussed in 'Methods, the MN size-dependent relationships in *Table 3* return eight $S_{mU} = k \cdot S_{MN}^c$ relationships between mU and MN properties (*Table 5*). A 2.8-fold range in positive c-values $c \in [2.4; 6.6]$ (mean 3.8 ± 1.5 sd) was obtained between studies. This result infers that mU and MN size are positively related in cats, mice, and potentially in rats.

Discussion

We processed the normalized data (*Figure 3*) from previous cat experimental studies to extract mathematical relationships (*Table 4*) between several MN electrophysiological and morphological properties (*Table 1*), providing a clear summary of previously known qualitative inter-relations between these MN properties. *Table 4* is a new convenient tool for neuroscientists, experimenters, and modellers. Besides obtaining significant quantitative correlations between MN electrophysiological properties and MN size (*Table 3*, *Figure 4*, *Figure 5*), we established (*Table 4*) and validated (*Figure 6*) a comprehensive mathematical framework that models an extensive set of experimental datasets available in the literature, quantitatively links all the pairs of the MN properties in *Table 1*, and is consistent with Rall's cable theory, as discussed in the following. This framework is directly applicable, although with limitations, to other mammalian species (*Figure 7*), and is used along with other measurements of mU properties (*Table 5*) to discuss the Henneman's size principle.

Consistency of the relationships with previous empirical results and Rall's theory

The mathematical relationships derived in *Table 4* are first in strong agreement with the relative variations between MN properties that were reported in review papers and are listed in 'Introduction'. Some combinations of the relationships in *Table 4* are besides consistent with other cat experimental data that were not included in the global datasets and were not used for deriving the relationships. For example, the relationships $I^{th} = k \cdot \tau^{-1.7}$, $\frac{1}{C} = k \cdot \tau^{0.7}$, $\frac{1}{S_{MN}} = k \cdot ACV^{-1.4}$, and $\frac{1}{R} = k \cdot ACV^{3.5}$ in *Table 4* yield, when combined, $\frac{I^{th}}{C} = k \cdot \tau^{-1}$ and $\frac{1}{R \cdot S_{MN}} = k \cdot ACV^{2.1}$, which are consistent with the relationship $\frac{I^{th}}{C} = k \cdot \tau^{-1}$ experimentally observed by *Gustafsson and Pinter, 1985* and $\frac{1}{R \cdot S_{MN}} = k \cdot ACV^{1.9}$ measured by *Kernell and Zwaagstra, 1981*. The stronger-than-linear inverse relationship $R = k \cdot S_{MN}^{-2.4}$ is also consistent with the phenomenological conclusions by *Kernell and Zwaagstra, 1981*. Moreover, some standard equations resulting from Rall's cable theory can be derived with a combination of the relationships in *Table 4*, assuming the MNs as equivalent cylinders with spatial uniformity of both C_m and R_m. For example, taking $\frac{\tanh(L)}{L} = 0.5$, which is in the typical $[0.48; 0.76]$ range reported in the literature (*Powers and Binder, 2001*), the relation $C = \frac{\tau}{R} \cdot \frac{L}{\tanh(L)}$ (eq. 1. in *Gustafsson and Pinter, 1984a*) is obtained when combining the $R - S_{neuron}$, $C - S_{neuron}$, and $\tau - S_{neuron}$ relationships. Also, taking $\frac{\tanh(L)}{L} = 0.6$ (standard value provided in *Powers and Binder, 2001*), the $R - S_{neuron}$ equation in *Table 4* applied to $R = \frac{R_m}{S_{neuron}} \cdot \frac{L}{\tanh(L)}$ in *Rall, 1977*, yields $R_m = \frac{1.0 \cdot 10^{-10}}{S_{neuron}^{1.4}}$. This $R_m - S_{neuron}$ relationship is consistent with the observations in *Powers and Binder, 2001* that smaller MNs have larger R_m values. Also, considering that $q_S^E = 2.4$ and $S_{neuron} \in [0.18; 0.44]$ mm^2 (*Appendix 1—table 3*), $R_m = \frac{1.0 \cdot 10^{-10}}{S_{MN}^{1.4}}$ makes R_m vary over the 3.5-fold theoretical range $[0.12; 0.44]$ $\Omega \cdot m^2$ in the MN pool. This is highly consistent both with the $q_A^E = 3.2$-fold range and the $[A_{min}^E; A_{max}^E] = [0.16; 0.59]$ $\Omega \cdot m^2$ mean range previously reported in the literature (*Albuquerque and Thesleff, 1968*; *Barrett and Crill, 1974*; *Burke et al., 1982*; *Gustafsson and Pinter, 1984b*). Also, $R_m = \frac{1.0 \cdot 10^{-10}}{S_{neuron}^{1.4}}$ yields $R_m = 2.5 \cdot AHP^{0.9}$ from the relationships in *Table 4*, which is consistent with the indirect conclusion of a positive correlation between R_m and AHP in *Gustafsson and Pinter, 1984b*. Finally, $R = \frac{0.6 R_m}{S_{neuron}}$ and $R_m = \frac{1.0 \cdot 10^{-10}}{S_{neuron}^{1.4}}$ support the statement that the variations in R_m in the MN pool may be as important as cell size S_{neuron} in determining MN excitability (*Gustafsson and Pinter, 1985*), although the variation of R in an MN pool may be also related to cell geometry (*Gustafsson and Pinter, 1984b*), which was not investigated in this study. This is consistent with the results in *Appendix 1—table 4*, which demonstrate that the range of variation q_S^E of S_{MN} does not entirely explain the ranges of variation q_R^E and $q_{I_{th}}^E$ of R and I_{th}, and that MN excitability is not only determined by MN size. Because of the aforementioned consistency with previous findings and with Rall's theory, the remaining relationships between R_m and the other MN properties were calculated from $R_m = \frac{1.0 \cdot 10^{-10}}{S_{neuron}^{1.4}}$, following the same methods as before, and added to *Table 4*. Importantly, R_m might however not be uniform across the somatodendritic membrane, according to results from completely reconstructed MNs (*Fleshman et al., 1988*), and might be positively correlated to the somatofugal distance (*Fleshman et al., 1983*), with dendritic R_m being higher than somatic R_m (*Barrett and Crill, 1974*; *Powers and Binder, 2001*; *Olinder et al., 2006*) by a factor 100–300 (*Clements and Redman, 1989*). This contradicts the assumptions of membrane isopotentiality necessary to apply Rall's cable theory. The relationships in *Table 4*, which were obtained from measurements in the soma where R_m is mainly constant, may thus not directly extrapolate to the dendritic regions of the MNs. Yet, the dimensionless variations of the average across MN surface of R_m with the other MN properties may still be valid (*Olinder et al., 2006*).

The equations in *Table 4* support the notion that MNs behave like resistive-capacitive systems, as demonstrated by the combination of the $R - \tau$ and $C - \tau$ relationships in *Table 4*, which yields $\tau^{0.9} = 0.8 \cdot RC$, close to the theoretical equation $\tau = RC \cdot \frac{\tanh(L)}{L}$ derived from Rall's theory. Also, *Table 4* directly yields, from the combination of $R_m = \frac{1.0 \cdot 10^{-10}}{S_{neuron}^{1.4}}$ with the other relationships, $\tau = 1.4 \cdot 10^{-2} \cdot R_m$, which is exactly eq. 2.15 in *Rall, 1977* ($\tau = R_m C_m$) with a constant value for $C_m = 1.4 \cdot 10^{-2} F \cdot m^{-2}$ that is consistent with the literature.

The relationship $C = 1.3 \cdot 10^{-2} \cdot S_{neuron}$ obtained in *Figure 4* and reported in *Table 4* is in agreement with the widely accepted proportional relationship between MN membrane capacitance and surface area, when spatial uniform values of R_m and C_m are assumed. It is worth noting that this proportional relationship was obtained in this study without simultaneous empirical measurements

of S_{MN} and C. The values of C were obtained from Rall's $C = \frac{\tau}{R} \cdot \frac{L}{\tanh(L)}$ equation (**Gustafsson and Pinter, 1984b**) and the corresponding values of S_{MN} were indirectly obtained from the final datasets $\{ACV; S_{MN}\}$, $\{AHP; S_{MN}\}$, $\{R; S_{MN}\}$ and $\{I_{th}; S_{MN}\}$ that involved the data from 17 selected studies as described in **Figure 1**. Although consistent with typical values reported in the literature (**Lux and Pollen, 1966**; **Albuquerque and Thesleff, 1968**; **Barrett and Crill, 1974**; **Adrian and Hodgkin, 1975**; **Sukhorukov et al., 1993**; **Major et al., 1994**; **Solsona et al., 1998**; **Thurbon et al., 1998**; **Gentet et al., 2000**), the $C_m = 1.3 \cdot 10^{-2} F \cdot m^{-2}$ constant value reported in this study is slightly higher than the widely accepted $C_m = 1.0 \cdot 10^{-2} F \cdot m^{-2}$ value (**Ulfhake and Kellerth, 1984**; **Gustafsson and Pinter, 1984b**). This high value is consistent with the conclusions from **Gustafsson and Pinter, 1984a**, who obtained slightly conservative values for S_{neuron} when approximating the MN surface area as $S_{neuron} = \frac{C}{C_m}$ with $C_m = 1.0 \cdot 10^{-2} F \cdot m^{-2}$.

Finally, the empirical relationship $I_{th} = \frac{2.7 \cdot 10^{-2}}{R^{1.0}}$ (**Table 4**) provides $\Delta V_{th} = 27 mV$, consistently with typical reported values (**Brock et al., 1952**; **Eccles et al., 1958a**), despite uncertainties in the value of the membrane resting potential (**Heckman and Enoka, 2012**) and lower values reported by **Gustafsson and Pinter, 1984a**. This supports the conclusions that the relative voltage threshold ΔV_{th} may be assumed constant within the MN pool in first approximation (**Coombs et al., 1955**; **Gustafsson and Pinter, 1984a**; **Powers and Binder, 2001**), and that Ohm's law is followed in MNs for weak subthreshold excitations (**Glenn and Dement, 1981**; **Ulfhake and Kellerth, 1984**; **Spruston and Johnston, 1992**; **Powers and Binder, 2001**; **Olinder et al., 2006**), as discussed in 'Methods'. However, voltage thresholds ΔV_{th} tend to be lower in in MNs of large R and long AHP (**Gustafsson and Pinter, 1984a**), suggesting that ΔV_{th} might be inversely correlated to MN size S_{MN}. Moreover, because of the voltage activation of persistent inward currents (PICs) near threshold which add to the external stimulating current and increases the MN input resistance (**Fleshman et al., 1988**), with a prominent effect on small MNs (**Powers and Binder, 2001**), the experimental values of ΔV_{th} are generally greater than that directly predicted from the product $I_{th} \cdot R$ (**Gustafsson and Pinter, 1984b**), and a variant of Ohm's law such as $\Delta V_{th}(V) = I_{th} \cdot R(V)$ should be considered during MN discharging events. This voltage-dependent variation in the values of R might partly explain why the range of the values of R reported in the literature for weak subthreshold currents (**Appendix 1—table 4**) is generally lower than that of I_{th}. While ΔV_{th} may be always size-dependent, and size-voltage-dependent close to threshold and during firing events, no correlation between $\frac{\Delta V_{th}}{R \cdot I_{th}}$ and C, AHP, or ACV was found and reported in **Table 4** in subthreshold conditions, consistent with measurements performed by **Gustafsson and Pinter, 1984b** and **Ulfhake and Kellerth, 1984**, substantiating that the dynamics of MN recruitment dominantly rely on R, I^{th}, and ΔV_{th} (**Heckman and Enoka, 2012**).

Relevance of the relationships

Table 4 provides the first quantitative description of an extensive set of cat experimental data available in the literature. These inter-related relationships were validated, successfully reconciliate the conclusions formulated by the selected experimental studies, and are in strong agreement with the theoretical equations describing Rall's cable theory. This robust framework advances our general understanding of the MN neurophysiology by inferring quantitative relationships for pairs of MN properties that were never concurrently measured in experiments (*Figure 2B*) by crossmatching other relationships involving these properties. For example, $I_{th} = 3.8 \cdot 10^8 \cdot S_{neuron}^{2.5}$ (*Table 4*) quantitatively supports the size dependency of I_{th} that was predicted by **Powers and Binder, 2001** from Rall's equations. Furthermore, modellers can directly and realistically tune with *Table 4* the physiological parameters of phenomenological MN models, such as leaky fire-and-integrate models, and/or build pools of MNs displaying a continuous distribution of realistic MN profiles of MN-specific electrophysiological and morphometric properties, as it has been previously attempted (**Dong et al., 2011**; **Negro et al., 2016**). Models tuned with *Table 4* can, for example, better replicate the discharging behaviour of MNs, obtained from decomposed high-density EMGs, than models scaled with generic property values (**Caillet et al., 2022**). In this view, such tuned models display MN-specific behaviours that should be easier to interpret. The mathematical relationships in *Table 4* can also support future experimental investigations performed on spinal MNs in adult mammals in vivo by completing experimental datasets for which properties that are difficult to measure were not obtained, such as the MN membrane time constant. Experimenters can therefore choose to reduce the workload of measuring

all the MN properties in *Table 1* to favour the identification of a maximum number of MNs and obtain extensive datasets describing larger MN populations that provide an informative window on the continuous distribution of MN properties in an MN pool. The unknown electrophysiological MN properties, typically obtained in vivo, of cadaveric specimens can also be estimated with the size-related relationships in *Table 4* from in vitro measurements of the somal diameter D_{soma} in a slice preparation of the spinal cord. The mathematical relationships in *Table 4* describe the experimental data published in the literature and provide a convenient metric for experimenters to compare their measurements to previous findings.

Extrapolation of the relationships to other mammals

It is demonstrated in *Figure 7* and with the calculation of the r^2 values in *Appendix 1—table 5* that the mathematical equations in *Table 4* obtained from cat data adequately predict the normalized associations between pairs of MN properties in rats and mice. However, the scaling factor K applied to the intercept k_e to scale the normalized relationships $A = K \cdot k_e \cdot B^e$ is species-specific, being, for example, around three times smaller in mice than in cat for the $\{\tau; R\}$ and $\{C; R\}$ pairs (*Figure 7*) and explaining the large *nRMSE* values in these cases. Absolute values of the $\{I_{th}; R\}$ pair were nevertheless accurately predicted in both rats and mice from the cat relationships, as explained by the larger values of R which counterbalances the respectively lower I_{th} values in mice and rats than in cats (*Manuel et al., 2019*; *Highlander et al., 2020*). Despite the age-related data variability (*Highlander et al., 2020*) in the rodent dataset displayed in *Figure 7*, these findings advance our understanding of the systematic inter-mammalian-species variations in MN properties. While the mathematical equations in *Table 4* are specific to cats, the normalized equations in *Appendix 1—table 2* can be scaled with species-specific data if investigating other mammals.

Henneman's size principle of motor unit recruitment

Table 5 reports statistically significant power relationships of positive power values between MN and mU indices of size. These results substantiate the concept that S_{MN} and S_{mU} are positively correlated in a motor unit (MU) pool and that large MNs innervate large mUs (*Henneman, 1981*; *Heckman and Enoka, 2012*), a statement that has never been demonstrated from the concurrent direct measurement of S_{MN} and S_{mU}. Besides, considering the positive $I_{th} - S_{MN}$ correlation (*Table 4*), and that the mU force recruitment threshold F^{th} is positively correlated to F^{tet} (*Heckman and Enoka, 2012*) and thus to S_{mU} (*Table 2*), larger MUs have both larger current and force recruitment thresholds I_{th} and F^{th} than relatively smaller MUs, which are thus recruited first, consistently with the Henneman's size principle of MU recruitment (*Henneman, 1957*; *Wuerker et al., 1965*; *Henneman et al., 1965a*; *Henneman et al., 1965b*; *Henneman et al., 1974*; *Henneman, 1981*; *Henneman, 1985*). The terminologies 'small MU', 'low-force MU', and 'low-threshold MU' are thus equivalent. Henneman's size principle thus relies on the amplitude of the MN membrane resistance (*Binder et al., 1996*; *Powers and Binder, 2001*; *Heckman and Enoka, 2012*). Finally, the relationships $S_{MN} \propto CV^{1.4} \propto \tau^{-0.7} \propto AHP^{-0.7}$ (*Table 4*) suggest that high-threshold MUs rely on relatively faster MN dynamics, which might partially explain why large MNs can attain relatively larger firing rates than low-thresholds MNs, for example, during ballistic contractions or during events close to maximum voluntary contractions (*Powers and Binder, 2001*; *Heckman and Enoka, 2012*).

It has been repeatedly attempted to extend Henneman's size principle and the correlations between the MU properties in *Table 1* to the concept of 'MU type' (*Burke and ten Bruggencate, 1971*; *Burke, 1981*; *Bakels and Kernell, 1993*; *Powers and Binder, 2001*). While a significant association between 'MU type' and indices of MU size has been observed in some animal (*Fleshman et al., 1981*; *Burke et al., 1982*; *Zengel et al., 1985*) and a few human (*Milner-Brown et al., 1973*; *Stephens and Usherwood, 1977*; *Garnett et al., 1979*; *Andreassen and Arendt-Nielsen, 1987*) studies, it has however not been observed in other animal studies (*Bigland-Ritchie et al., 1998* for a review) and in the majority of human investigations (*Sica and McComas, 1971*; *Goldberg and Derfler, 1977*; *Yemm, 1977*; *Young and Mayer, 1982*; *Thomas et al., 1990*; *Nordstrom and Miles, 1990*; *Elek et al., 1992*; *Macefield et al., 1996*; *Van Cutsem et al., 1997*; *Mateika et al., 1998*; *Fuglevand et al., 1999*; *Keen and Fuglevand, 2004*). Moreover, the reliability of these results is weakened by the strong limitations of the typical MU-type identification protocols. Sag experiments are irrelevant in humans (*Buchthal and Schmalbruch, 1970*; *Thomas et al., 1991*; *Bakels and Kernell, 1993*; *Macefield et al.,*

1996; *Bigland-Ritchie et al., 1998*; *Fuglevand et al., 1999*) and lack consistency with other identification methods (*Nordstrom and Miles, 1990*). MU-type identification by twitch contraction time measurements is limited by the strong sources of inaccuracy involved in the transcutaneous stimulation, intramuscular microstimulation, intraneural stimulation, and spike-triggered averaging techniques (*Taylor et al., 2002*; *Keen and Fuglevand, 2004*; *McNulty and Macefield, 2005*; *Negro et al., 2014*; *Dideriksen and Negro, 2018*). Finally, as muscle fibres show a continuous distribution of contractile properties among the MU pool, some MUs fail to be categorized in discrete MU types in some animal studies by histochemical approaches (*Reinking et al., 1975*; *Tötösy de Zepetnek et al., 1992*). Owing to these conflicting results and technical limitations, MU type may not be related to MN size and the basis for MU recruitment during voluntary contractions (*McNulty and Macefield, 2005*; *Duchateau and Enoka, 2011*).

Limitations

The mathematical relationships derived *Table 4* and the conclusions drawn in 'Discussion' present some limitations, most of which were previously discussed and are summarised here. A first limitation relates to the experimental inaccuracies in measuring the MN properties in *Table 1*. As discussed, the true values of R and τ, and thus of R_m and C, may be underestimated because of a membrane leak conductance around the electrode and some voltage-activated membrane nonlinearities. Yet, the selected studies reduced the impact of these phenomena, which besides may not affect the association between MN properties (*Gustafsson and Pinter, 1984a*). Also, τ, C, and R_m were estimated assuming that the MN membrane is isopotential. This is valid in the soma, where τ, C, and R_m were measured, and the relationships in *Table 4* are adequate for an MN simplified to one equivalent cable. However, as the membrane resistivity may increase with somatofugal distance, as discussed previously, the relationships in *Table 4* may be offset towards larger R values in dendritic areas, which should be accounted for when modelling the MN dendrites in compartmental MN models or completely reconstructed dendritic trees. Finally, the selected cat studies are relatively dated, as observed in *Manuel et al., 2019*. Thus, recent computer-assisted techniques of MN morphometric measurements were notably not applicable in those studies, yielding important sources of inaccuracies, as discussed in Appendix 1. Therefore, the relationships involving S_{neuron} are subjected to a higher level of inaccuracy. A second limitation arises from the inter-study variability of the experimental datasets reported in the selected studies. As discussed, animal preparations slightly diverged between the selected studies. Also, because of the scarcity of available data in the literature, measurements obtained from MNs innervating different muscles from adult animals of different sex and age were merged into unique datasets. This inter-study variability, added to the 'unexplained' variance reported in *Highlander et al., 2020*, was however reduced by the normalization of the experimental datasets, as investigated in *Appendix 1—figures 2 and 4*. The normalization approach is however only valid if the experimental studies identified the same largest MN relatively to the MN populations under investigation. This cannot be verified but is likely as most studies returned similar normalized distributions of their measured parameters, as displayed in *Appendix 1—figure 1*, inferring that a similar portion of the MN pools was identified in the selected studies. Finally, the results proposed in this study may be affected by methodological bias from the three research groups that provided most of the data points processed in this study, even if all the selected studies reported similar methods to measure the properties, as discussed in 'Methods'.

A third limitation is due to the limited processable experimental data available in the literature, especially in rats and mice, as also discussed by *Heckman and Enoka, 2012*. The extrapolation of the relationships in *Table 4* to rat and mouse species could only be assessed against a small set of studies and for three associations only. The conclusions on the associations between S_{mU} and S_{MN} also relied on few studies providing few measurements due to the considerable amount of work required to measure both MN and mU properties in single MUs. In cats, some pairs of MN properties were investigated in only one study, preventing inter-study comparisons, and stressing the usefulness of *Table 4* for reconciliating the data available in the literature. Within the experimental datasets, the scarcity of data points in some regions of the data distributions (e.g., see the skewed I_{th} and R distributions in the density histograms in *Appendix 1—figure 1*) transfers during processing to the final size-dependent datasets (*Figure 4*). This data heterogeneity may affect the reliability of the relationships in *Table 4* for the extreme MN sizes (see, in *Figure 4*, the 95% confidence interval of the regressions widening for

small S_{MN} in the $\{AHP; S_{MN}\}$ and $\{R; S_{MN}\}$ datasets and for large S_{MN} in the $\{I_{th}; S_{MN}\}$ dataset). In the validation procedure, the highest nME values reported in *Figure 6* were obtained for these regions of limited data for most of the global datasets. This heterogeneous density of the data may be explained by the natural skewness of the MN property distributions in the MN pool towards many small MNs and few large MNs (*Heckman and Enoka, 2012*) and/or a systematic experimental bias towards identifying and investigating relatively large MUs.

A fourth limitation arises from the relatively low r^2 values obtained from the power regressions in *Table 3*. Although these power trendlines are statistically significant (see p-values in *Table 3*) and globally provide a better description of the data than other fits (see *Appendix 1—table 1*), they cannot entirely describe the associations between MN property distributions, in line with the conclusions reported in the selected studies. According to these first four limitations, the mathematical relationships in *Table 4* best reproduce published cat data but include the level of inaccuracies of the original experimental approaches.

A fifth limitation is the restriction of the study to the MN properties reported in *Table 1*. Other MN-specific properties, such as the electronic length, the relationship between discharge rate and excitatory current and its hysteresis, or the amplitude of the inhibitory and excitatory postsynaptic potentials, were omitted because they were rarely measured or reported along with S_{MN}, ACV, AHP, R, I_{th}, C, and τ in the selected studies. Moreover, as the cell geometry was not investigated in this study, other MN properties (*Clements and Redman, 1989*) such as the effects of the distributed synaptic integration along the dendritic tree were overlooked. Finally, apart from I_{th}, ACV, and AHP, all the MN properties investigated in this study are passive properties, that is, baseline properties of the cell at rest (*Powers and Binder, 2001*), as they were measured using weak sub-threshold current pulses. Therefore, other MN active properties, such as voltage-dependent ionic channel-related properties including PICs, which activate close or above threshold, were not considered in this study. While this limits the applicability of *Table 4* to a functional context or in comprehensive Hodgkin–Huxley-like models of MNs, some relationships in *Table 4* remain pertinent in those conditions if they are linked with other observations in the literature on MN active properties, for example, MNs of small S_{MN} having longer lasting total PICs of greater hyperpolarized activation than MNs of large S_{MN} (*Heckman and Enoka, 2012*). Despite the aforementioned limitations, the relationships in *Table 4* can be directly used in phenomenological RC approaches like LIF models (*Izhikevich, 2004*; *Teeter et al., 2018*), which rely on the properties reported in *Table 1*, to derive profiles of inter-consistent MN-specific properties and describe realistic continuous distributions of the MN properties R, I_{th}, C, ΔV_{th}, and τ in the MN pool, as attempted in previous works (*Dong et al., 2011*; *Negro et al., 2016*). An example of a computational modelling application of *Table 4* is provided in *Caillet et al., 2022*, where the relationships tune a cohort of LIF models which estimate, from the firing activity of a portion of the MN pool obtained from decomposed high-density EMGs, a realistic distribution of the MN properties in the MN pool and the firing behaviour of a complete MN pool in an isometrically contracting human muscle.

As a final limitation, the relationships in *Table 4* were obtained from a regression analysis and therefore provide correlations between some MN properties in an MN pool but cannot be used to draw conclusions on the causality behind these associations.

Conclusion

This study provides in *Table 4* a mathematical framework of quantitative associations between the MN properties S_{MN}, ACV, AHP, R, R_m, I_{th}, C, and τ. This framework, which is consistent with most of the empirical and theoretical conclusions in the literature, clarifies our understanding of the association between these MN properties and constitutes a convenient tool for neuroscientists, experimenters, and modellers to generate hypotheses for experimental studies aiming at investigating currently unreported relationships, support experimentations, and build virtual MN profiles of inter-consistent MN-specific properties for MN modelling purposes.

Acknowledgements

the experimental data published in Huh et al., 2021, Time course of alterations in adult spinal moto-neuron properties in the SOD1 (G93A) mouse model of ALS, Eneuro.

Additional information

Funding

Author contributions

Author ORCIDs

Arnault H Caillet https://orcid.org/0000-0001-6146-1829
Andrew TM Phillips https://orcid.org/0000-0001-6618-0145
Dario Farina https://orcid.org/0000-0002-7883-2697
Luca Modenese https://orcid.org/0000-0003-1402-5359

Decision letter and Author response

Decision letter https://doi.org/10.7554/eLife.76489.sa1
Author response https://doi.org/10.7554/eLife.76489.sa2

Additional files

Supplementary files

• Transparent reporting form

Data availability

Figure 3 - Source Data 1 contains the numerical data used to generate Figure 3. Figure 7 - Source Data 1 and Figure 7 - Source Data 2 contain the numerical data used to generate Figure 7. Table 5 - Source Data 1 contains the numerical data used to compute the mathematical relationships presented in Table 5. Please note that our study used exclusively data from previous investigations, for which public datasets were not available. The data were manually digitised by the authors from published figures and are made available as supplementary materials.

References

Adrian RH, Hodgkin AL. 1975. Conduction velocity and gating current in the squid giant axon. *Proceedings of the Royal Society of London. Series B, Biological Sciences* **189**:81–86. DOI: https://doi.org/10.1098/rspb.1975.0043, PMID: 237279

Albuquerque EX, Thesleff S. 1968. A comparative study of membrane properties of innervated and chronically denervated fast and slow skeletal muscles of the rat. *Acta Physiologica Scandinavica* **73**:471–480. DOI: https://doi.org/10.1111/j.1365-201x.1968.tb10886.x, PMID: 5708174

Amendola J, Durand J. 2008. Morphological differences between wild-type and transgenic superoxide dismutase 1 lumbar motoneurons in postnatal mice. *The Journal of Comparative Neurology* **511**:329–341. DOI: https://doi.org/10.1002/cne.21818, PMID: 18803237

Andreassen S, Arendt-Nielsen L. 1987. Muscle fibre conduction velocity in motor units of the human anterior tibial muscle: A new size principle parameter. *The Journal of Physiology* **391**:561–571. DOI: https://doi.org/10.1113/jphysiol.1987.sp016756, PMID: 3443957

Ankit R. 2020. WebPlotDigitizer. 4.4. https://automeris.io/WebPlotDigitizer

Appelberg B, Emonet-Dénand F. 1967. Motor units of the first superficial lumbrical muscle of the cat. *Journal of Neurophysiology* **30**:154–160. DOI: https://doi.org/10.1152/jn.1967.30.1.154

Bagust J. 1974. Relationships between motor nerve conduction velocities and motor unit contraction characteristics in a slow twitch muscle of the cat. *The Journal of Physiology* **238**:269–278. DOI: https://doi.org/10.1113/jphysiol.1974.sp010523, PMID: 4840992

Bakels R, Kernell D. 1993. Matching between motoneurone and muscle unit properties in rat medial gastrocnemius. *The Journal of Physiology* **463**:307–324. DOI: https://doi.org/10.1113/jphysiol.1993.sp019596, PMID: 8246185

Barrett JN, Crill WE. 1974. Specific membrane properties of cat motoneurones. *The Journal of Physiology* **239**:301–324. DOI: https://doi.org/10.1113/jphysiol.1974.sp010570, PMID: 4137933

Bigland-Ritchie B, Fuglevand AJ, Thomas CK. 1998. Contractile properties of human motor units: is man a cat? *The Neuroscientist* **4**:240–249. DOI: https://doi.org/10.1177/107385849800400413

Binder MD, Heckman CJ, Powers RK. 1996. The physiological control of motoneuron activity. RowellLB (Ed). *Handbook of Physiology: Exercise, Regulation and Integration of Multiple Systems.* New York: Oxford Univ Press. p. 3–53.

Bodine SC, Roy RR, Eldred E, Edgerton VR. 1987. Maximal force as a function of anatomical features of motor units in the cat tibialis anterior. *Journal of Neurophysiology* **57**:1730–1745. DOI: https://doi.org/10.1152/jn.1987.57.6.1730, PMID: 3598628

Brandenburg JE, Gransee HM, Fogarty MJ, Sieck GC. 2018. Differences in lumbar motor neuron pruning in an animal model of early onset spasticity. *Journal of Neurophysiology* **120**:601–609. DOI: https://doi.org/10.1152/jn.00186.2018, PMID: 29718808

Brandenburg JE, Fogarty MJ, Brown AD, Sieck GC. 2020. Phrenic motor neuron loss in an animal model of early onset hypertonia. *Journal of Neurophysiology* **123**:1682–1690. DOI: https://doi.org/10.1152/jn.00026.2020, PMID: 32233911

Brock LG, Coombs JS, Eccles JC. 1952. The recording of potentials from motoneurones with an intracellular electrode. *The Journal of Physiology* **117**:431–460. DOI: https://doi.org/10.1113/jphysiol.1952.sp004759, PMID: 12991232

Buchthal F, Schmalbruch H. 1970. Contraction times and fibre types in intact human muscle. *Acta Physiologica Scandinavica* **79**:435–452. DOI: https://doi.org/10.1111/j.1748-1716.1970.tb04744.x, PMID: 5472111

Burke RE. 1968. Firing patterns of gastrocnemius motor units in the decerebrate cat. *The Journal of Physiology* **196**:631–654. DOI: https://doi.org/10.1113/jphysiol.1968.sp008527, PMID: 5664235

Burke RE, ten Bruggencate G. 1971. Electrotonic characteristics of alpha motoneurones of varying size. *The Journal of Physiology* **212**:1–20. DOI: https://doi.org/10.1113/jphysiol.1971.sp009307

Burke RE, Tsairis P. 1973. Anatomy and innervation ratios in motor units of cat gastrocnemius. *The Journal of Physiology* **234**:749–765. DOI: https://doi.org/10.1113/jphysiol.1973.sp010370, PMID: 4148753

Burke RE. 1981. Motor units: anatomy, physiology, and functional organization. Brooks VB (Ed). *Handbook of Physiology, the Nervous System, Motor Control.* American Physiological Society. p. 345–422.

Burke RE, Dum RP, Fleshman JW, Glenn LL, Lev-Tov A, O'Donovan MJ, Pinter MJ. 1982. A HRP study of the relation between cell size and motor unit type in cat ankle extensor motoneurons. *The Journal of Comparative Neurology* **209**:17–28. DOI: https://doi.org/10.1002/cne.902090103, PMID: 7119171

Button DC, Kalmar JM, Gardiner K, Marqueste T, Zhong H, Roy RR, Edgerton VR, Gardiner PF. 2008. Does elimination of afferent input modify the changes in rat motoneurone properties that occur following chronic spinal cord transection? *The Journal of Physiology* **586**:529–544. DOI: https://doi.org/10.1113/jphysiol.2007.141499, PMID: 18006586

Caillet AH, Phillips ATM, Farina D, Modenese L. 2022. Estimation of the firing behaviour of a complete motoneuron pool by combining electromyography signal decomposition and realistic motoneuron modelling. *PLOS Computational Biology* **18**:e1010556. DOI: https://doi.org/10.1371/journal.pcbi.1010556, PMID: 36174126

Carp JS, Tennissen AM, Mongeluzi DL, Dudek CJ, Chen XY, Wolpaw JR. 2008. An in vitro protocol for recording from spinal motoneurons of adult rats. *Journal of Neurophysiology* **100**:474–481. DOI: https://doi.org/10.1152/jn.90422.2008, PMID: 18463177

Carrascal L, Nieto-Gonzalez JL, Torres B, Nunez-Abades P. 2009. Changes in somatodendritic morphometry of rat oculomotor nucleus motoneurons during postnatal development. *The Journal of Comparative Neurology* **514**:189–202. DOI: https://doi.org/10.1002/cne.21996, PMID: 19274669

Chamberlain S, Lewis DM. 1989. Contractile characteristics and innervation ratio of rat soleus motor units. *The Journal of Physiology* **412**:1–21. DOI: https://doi.org/10.1113/jphysiol.1989.sp017601, PMID: 2600827

Chollet F. 2021. Deep Learning with Python. Simon and Schuster.

Clements JD, Redman SJ. 1989. Cable properties of cat spinal motoneurones measured by combining voltage clamp, current clamp and intracellular staining. *The Journal of Physiology* **409**:63–87. DOI: https://doi.org/10.1113/jphysiol.1989.sp017485, PMID: 2585300

Coombs JS, Eccles JC, Fatt P. 1955. The electrical properties of the motoneurone membrane. *The Journal of Physiology* **130**:291–325. DOI: https://doi.org/10.1113/jphysiol.1955.sp005411, PMID: 13278904

Copray S, Kernell D. 2000. Neurotrophins and trk-receptors in adult rat spinal motoneurons: differences related to cell size but not to "slow/fast" specialization. *Neuroscience Letters* **289**:217–220. DOI: https://doi.org/10.1016/s0304-3940(00)01305-7, PMID: 10961668

Cullheim S. 1978. Relations between cell body size, axon diameter and axon conduction velocity of cat sciatic alpha-motoneurons stained with horseradish peroxidase. *Neuroscience Letters* **8**:17–20. DOI: https://doi.org/10.1016/0304-3940(78)90090-3, PMID: 19605142

Cullheim S, Fleshman JW, Glenn LL, Burke RE. 1987. Membrane area and dendritic structure in type-identified triceps surae alpha motoneurons. *The Journal of Comparative Neurology* **255**:68–81. DOI: https://doi.org/10.1002/cne.902550106, PMID: 3819010

Deardorff AS, Romer SH, Deng Z, Bullinger KL, Nardelli P, Cope TC, Fyffe REW. 2013. Expression of postsynaptic Ca2+-activated K+ (SK) channels at C-bouton synapses in mammalian lumbar -motoneurons. *The Journal of Physiology* **591**:875–897. DOI: https://doi.org/10.1113/jphysiol.2012.240879, PMID: 23129791

Delestrée N, Manuel M, Iglesias C, Elbasiouny SM, Heckman CJ, Zytnicki D. 2014. Adult spinal motoneurones are not hyperexcitable in a mouse model of inherited amyotrophic lateral sclerosis. *The Journal of Physiology* **592**:1687–1703. DOI: https://doi.org/10.1113/jphysiol.2013.265843, PMID: 24445319

Destombes J, Horcholle-Bossavit G, Thiesson D, Jami L. 1992. Alpha and gamma motoneurons in the peroneal nuclei of the cat spinal cord: an ultrastructural study. *The Journal of Comparative Neurology* **317**:79–90. DOI: https://doi.org/10.1002/cne.903170106, PMID: 1573058

Dideriksen JL, Negro F. 2018. Spike-triggered averaging provides inaccurate estimates of motor unit twitch properties under optimal conditions. *Journal of Electromyography and Kinesiology* **43**:104–110. DOI: https://doi.org/10.1016/j.jelekin.2018.09.008, PMID: 30267966

Dong Y, Mihalas S, Russell A, Etienne-Cummings R, Niebur E. 2011. Estimating parameters of generalized integrate-and-fire neurons from the maximum likelihood of spike trains. *Neural Computation* **23**:2833–2867. DOI: https://doi.org/10.1162/NECO_a_00196, PMID: 21851282

Donselaar Y, Kernell D, Eerbeek O. 1986. Soma size and oxidative enzyme activity in normal and chronically stimulated motoneurones of the cat's spinal cord. *Brain Research* **385**:22–29. DOI: https://doi.org/10.1016/0006-8993(86)91542-8, PMID: 3768720

Duchateau J, Enoka RM. 2011. Human motor unit recordings: origins and insight into the integrated motor system. *Brain Research* **1409**:42–61. DOI: https://doi.org/10.1016/j.brainres.2011.06.011, PMID: 21762884

Dukkipati SS, Garrett TL, Elbasiouny SM. 2018. The vulnerability of spinal motoneurons and soma size plasticity in a mouse model of amyotrophic lateral sclerosis. *The Journal of Physiology* **596**:1723–1745. DOI: https://doi.org/10.1113/JP275498, PMID: 29502344

Dum RP, Kennedy TT. 1980. Physiological and histochemical characteristics of motor units in cat tibialis anterior and extensor digitorum longus muscles. *Journal of Neurophysiology* **43**:1615–1630. DOI: https://doi.org/10.1152/jn.1980.43.6.1615, PMID: 6447772

Eccles JC, Eccles RM, Lundberg A. 1957. Durations of after-hyperpolarization of motoneurones supplying fast and slow muscles. *Nature* **179**:866–868. DOI: https://doi.org/10.1038/179866b0, PMID: 13430719

Eccles JC, Eccles RM, Lundberg A. 1958a. The action potentials of the alpha motoneurones supplying fast and slow muscles. *The Journal of Physiology* **142**:275–291. DOI: https://doi.org/10.1113/jphysiol.1958.sp006015, PMID: 13564435

Eccles JC, Libet B, Young RR. 1958b. The behaviour of chromatolysed motoneurones studied by intracellular recording. *The Journal of Physiology* **143**:11–40. DOI: https://doi.org/10.1113/jphysiol.1958.sp006041, PMID: 13576457

Elek JM, Kossev A, Dengler R, Schubert M, Wohlfahrt K, Wolf W. 1992. Parameters of human motor unit twitches obtained by intramuscular microstimulation. *Neuromuscular Disorders* **2**:261–267. DOI: https://doi.org/10.1016/0960-8966(92)90058-e, PMID: 1483052

Emonet-Dénand F, Hunt CC, Petit J, Pollin B. 1988. Proportion of fatigue-resistant motor units in hindlimb muscles of cat and their relation to axonal conduction velocity. *The Journal of Physiology* **400**:135–158. DOI: https://doi.org/10.1113/jphysiol.1988.sp017115, PMID: 3418525

Enoka RM. 1995. Morphological features and activation patterns of motor units. *Journal of Clinical Neurophysiology* **12**:538–559. DOI: https://doi.org/10.1097/00004691-199511000-00002, PMID: 8600170

Filipchuk AA, Durand J. 2012. Postnatal dendritic development in lumbar motoneurons in mutant superoxide dismutase 1 mouse model of amyotrophic lateral sclerosis. *Neuroscience* **209**:144–154. DOI: https://doi.org/10.1016/j.neuroscience.2012.01.046, PMID: 22387111

Fleshman JW, Munson JB, Sypert GW, Friedman WA. 1981. Rheobase, input resistance, and motor-unit type in medial gastrocnemius motoneurons in the cat. *Journal of Neurophysiology* **46**:1326–1338. DOI: https://doi.org/10.1152/jn.1981.46.6.1326, PMID: 6275043

Fleshman JW, Segev I, Cullheim S, Burke RE. 1983. Matching electrophysiological with morphological measurements in cat α-motoneurons. In Soc. Neurosci. Abstr (Vol. 9, p. 431).

Fleshman JW, Segev I, Burke RB. 1988. Electrotonic architecture of type-identified alpha-motoneurons in the cat spinal cord. *Journal of Neurophysiology* **60**:60–85. DOI: https://doi.org/10.1152/jn.1988.60.1.60, PMID: 3404225

Foehring RC, Sypert GW, Munson JB. 1986. Properties of self-reinnervated motor units of medial gastrocnemius of cat. II. Axotomized motoneurons and time course of recovery. *Journal of Neurophysiology* **55**:947–965. DOI: https://doi.org/10.1152/jn.1986.55.5.947, PMID: 3711974

Foehring RC, Sypert GW, Munson JB. 1987. Motor-unit properties following cross-reinnervation of cat lateral gastrocnemius and soleus muscles with medial gastrocnemius nerve. II. Influence of muscle on motoneurons. *Journal of Neurophysiology* **57**:1227–1245. DOI: https://doi.org/10.1152/jn.1987.57.4.1227, PMID: 3585462

Frank K, Fuortes MG. 1956. Stimulation of spinal motoneurones with intracellular electrodes. *The Journal of Physiology* **134**:451–470. DOI: https://doi.org/10.1113/jphysiol.1956.sp005657, PMID: 13398925

Friese A, Kaltschmidt JA, Ladle DR, Sigrist M, Jessell TM, Arber S. 2009. Gamma and alpha motor neurons distinguished by expression of transcription factor Err3. *PNAS* **106**:13588–13593. DOI: https://doi.org/10.1073/pnas.0906809106, PMID: 19651609

Fuglevand AJ, Macefield VG, Bigland-Ritchie B. 1999. Force-frequency and fatigue properties of motor units in muscles that control digits of the human hand. *Journal of Neurophysiology* **81**:1718–1729. DOI: https://doi.org/10.1152/jn.1999.81.4.1718, PMID: 10200207

Gao H, Glatzer NR, Williams KW, Derbenev AV, Liu D, Smith BN. 2009. Morphological and electrophysiological features of motor neurons and putative interneurons in the dorsal vagal complex of rats and mice. *Brain Research* **1291**:40–52. DOI: https://doi.org/10.1016/j.brainres.2009.07.024, PMID: 19619517

Gardiner PF. 1993. Physiological properties of motoneurons innervating different muscle unit types in rat gastrocnemius. *Journal of Neurophysiology* **69**:1160–1170. DOI: https://doi.org/10.1152/jn.1993.69.4.1160, PMID: 8492155

Garnett RAF, O'Donovan MJ, Stephens JA, Taylor A. 1979. Motor unit organization of human medial gastrocnemius. *The Journal of Physiology* **287**:33–43. DOI: https://doi.org/10.1113/jphysiol.1979.sp012643, PMID: 430414

Gentet LJ, Stuart GJ, Clements JD. 2000. Direct measurement of specific membrane capacitance in neurons. *Biophysical Journal* **79**:314–320. DOI: https://doi.org/10.1016/S0006-3495(00)76293-X, PMID: 10866957

Glenn LL, Dement WC. 1981. Membrane resistance and rheobase of hindlimb motoneurons during wakefulness and sleep. *Journal of Neurophysiology* **46**:1076–1088. DOI: https://doi.org/10.1152/jn.1981.46.5.1076, PMID: 7299447

Goldberg LJ, Derfler B. 1977. Relationship among recruitment order, spike amplitude, and twitch tension of single motor units in human masseter muscle. *Journal of Neurophysiology* **40**:879–890. DOI: https://doi.org/10.1152/jn.1977.40.4.879, PMID: 886372

Gustafsson B. 1979. Changes in motoneurone electrical properties following axotomy. *The Journal of Physiology* **293**:197–215. DOI: https://doi.org/10.1113/jphysiol.1979.sp012885, PMID: 501587

Gustafsson B, Pinter MJ. 1984a. An investigation of threshold properties among cat spinal alpha-motoneurones. *The Journal of Physiology* **357**:453–483. DOI: https://doi.org/10.1113/jphysiol.1984.sp015511, PMID: 6512700

Gustafsson B, Pinter MJ. 1984b. Relations among passive electrical properties of lumbar alpha-motoneurones of the cat. *The Journal of Physiology* **356**:401–431. DOI: https://doi.org/10.1113/jphysiol.1984.sp015473, PMID: 6520792

Gustafsson B, Pinter MJ. 1985. On factors determining orderly recruitment of motor units: A role for intrinsic membrane properties. *Trends in Neurosciences* **8**:431–433. DOI: https://doi.org/10.1016/0166-2236(85)90152-3

Heckman CJ, Enoka RM. 2012. Motor unit. *Comprehensive Physiology* **2**:2629–2682. DOI: https://doi.org/10.1002/cphy.c100087, PMID: 23720261

Hegedus J, Putman CT, Gordon T. 2007. Time course of preferential motor unit loss in the SOD1 G93A mouse model of amyotrophic lateral sclerosis. *Neurobiology of Disease* **28**:154–164. DOI: https://doi.org/10.1016/j.nbd.2007.07.003, PMID: 17766128

Henneman E. 1957. Relation between size of neurons and their susceptibility to discharge. *Science* **126**:1345–1347. DOI: https://doi.org/10.1126/science.126.3287.1345, PMID: 13495469

Henneman E, Somjen G, Carpenter DO. 1965a. Functional significance of cell size in spinal motoneurons. *Journal of Neurophysiology* **28**:560–580. DOI: https://doi.org/10.1152/jn.1965.28.3.560, PMID: 14328454

Henneman E, Somjen G, Carpenter DO. 1965b. Excitability and inhibitibility of motoneurons of different sizes. *Journal of Neurophysiology* **28**:599–620. DOI: https://doi.org/10.1152/jn.1965.28.3.599, PMID: 5835487

Henneman E, Clamann HP, Gillies JD, Skinner RD. 1974. Rank order of motoneurons within a pool: law of combination. *Journal of Neurophysiology* **37**:1338–1349. DOI: https://doi.org/10.1152/jn.1974.37.6.1338, PMID: 4436704

Henneman E. 1981. Recruitment of motoneurons: the size principle. *Motor Unit Types, Recruitment and Plasticity in Health and Disease* 26–60.

Henneman E. 1985. The size-principle: A deterministic output emerges from A set of probabilistic connections. *The Journal of Experimental Biology* **115**:105–112. DOI: https://doi.org/10.1242/jeb.115.1.105, PMID: 3161974

Highlander MM, Allen JM, Elbasiouny SM. 2020. Meta-analysis of biological variables' impact on spinal motoneuron electrophysiology data. *Journal of Neurophysiology* **123**:1380–1391. DOI: https://doi.org/10.1152/jn.00378.2019, PMID: 32073942

Huh S, Heckman CJ, Manuel M. 2021. Time Course of Alterations in Adult Spinal Motoneuron Properties in the SOD1(G93A) Mouse Model of ALS. *ENeuro* **8**:ENEURO.0378-20.2021. DOI: https://doi.org/10.1523/ENEURO.0378-20.2021, PMID: 33632815

Ishihara A, Kawano F, Ishioka N, Oishi H, Higashibata A, Shimazu T, Ohira Y. 2001. Growth-related changes in cell body size and succinate dehydrogenase activity of spinal motoneurons innervating the rat soleus muscle. *International Journal of Developmental Neuroscience* **21**:461–469. DOI: https://doi.org/10.1016/j.ijdevneu.2003.08.003, PMID: 14659997

Issa AN, Zhan WZ, Sieck GC, Mantilla CB. 2010. Neuregulin-1 at synapses on phrenic motoneurons. *The Journal of Comparative Neurology* **518**:4213–4225. DOI: https://doi.org/10.1002/cne.22449, PMID: 20878784

Ito M, Oshima T. 1965. Electrical behaviour of the motoneurone membrane during intracellularly applied current steps. *The Journal of Physiology* **180**:607–635. DOI: https://doi.org/10.1113/jphysiol.1965.sp007720

Izhikevich EM. 2004. Which model to use for cortical spiking neurons? *IEEE Transactions on Neural Networks* **15**:1063–1070. DOI: https://doi.org/10.1109/TNN.2004.832719, PMID: 15484883

Jami L, Petit J. 1975. Correlation between axonal conduction velocity and tetanic tension of motor units in four muscles of the cat hind limb. *Brain Research* **96**:114–118. DOI: https://doi.org/10.1016/0006-8993(75)90581-8, PMID: 1174992

Kanda K, Hashizume K. 1992. Factors causing difference in force output among motor units in the rat medial gastrocnemius muscle. *The Journal of Physiology* **448**:677–695. DOI: https://doi.org/10.1113/jphysiol.1992.sp019064, PMID: 1593483

Kanjhan R, Fogarty MJ, Noakes PG, Bellingham MC. 2015. Developmental changes in the morphology of mouse hypoglossal motor neurons. *Brain Structure & Function* **221**:3755–3786. DOI: https://doi.org/10.1007/s00429-015-1130-8, PMID: 26476929

Keen DA, Fuglevand AJ. 2004. Distribution of motor unit force in human extensor digitorum assessed by spike-triggered averaging and intraneural microstimulation. *Journal of Neurophysiology* **91**:2515–2523. DOI: https://doi.org/10.1152/jn.01178.2003, PMID: 14724266

Kernell D. 1966. Input resistance, electrical excitability, and size of ventral horn cells in cat spinal cord. Science **152**:1637–1640. DOI: https://doi.org/10.1126/science.152.3729.1637, PMID: 5936887

Kernell D, Monster AW. 1981. Threshold current for repetitive impulse firing in motoneurones innervating muscle fibres of different fatigue sensitivity in the cat. *Brain Research* **229**:193–196. DOI: https://doi.org/10.1016/0006-8993(81)90756-3, PMID: 7306807

Kernell D, Zwaagstra B. 1981. Input conductance axonal conduction velocity and cell size among hindlimb motoneurones of the cat. *Brain Research* **204**:311–326. DOI: https://doi.org/10.1016/0006-8993(81)90591-6, PMID: 7459634

Knott S, Lewis DM, Luck JC. 1971. Motor unit areas in a cat limb muscle. *Experimental Neurology* **30**:475–483. DOI: https://doi.org/10.1016/0014-4886(71)90148-8, PMID: 4251992

Krawitz S, Fedirchuk B, Dai Y, Jordan LM, McCrea DA. 2001. State-dependent hyperpolarization of voltage threshold enhances motoneurone excitability during fictive locomotion in the cat. *The Journal of Physiology* **532**:271–281. DOI: https://doi.org/10.1111/j.1469-7793.2001.0271g.x, PMID: 11283241

Krutki P, Hałuszka A, Mrówczyński W, Gardiner PF, Celichowski J. 2015. Adaptations of motoneuron properties to chronic compensatory muscle overload. *Journal of Neurophysiology* **113**:2769–2777. DOI: https://doi.org/10.1152/jn.00968.2014, PMID: 25695651

Lee RH, Heckman CJ. 1998. Bistability in spinal motoneurons in vivo: systematic variations in persistent inward currents. *Journal of Neurophysiology* **80**:583–593. DOI: https://doi.org/10.1152/jn.1998.80.2.583, PMID: 9705452

Li Y, Brewer D, Burke RE, Ascoli GA. 2005. Developmental changes in spinal motoneuron dendrites in neonatal mice. *The Journal of Comparative Neurology* **483**:304–317. DOI: https://doi.org/10.1002/cne.20438, PMID: 15682391

Lucas SM, Ruff RL, Binder MD. 1987. Specific tension measurements in single soleus and medial gastrocnemius muscle fibers of the cat. *Experimental Neurology* **95**:142–154. DOI: https://doi.org/10.1016/0014-4886(87)90013-6, PMID: 2947808

Lux HD, Pollen DA. 1966. Electrical constants of neurons in the motor cortex of the cat. *Journal of Neurophysiology* **29**:207–220. DOI: https://doi.org/10.1152/jn.1966.29.2.207, PMID: 5927458

Macefield VG, Fuglevand AJ, Bigland-Ritchie B. 1996. Contractile properties of single motor units in human toe extensors assessed by intraneural motor axon stimulation. *Journal of Neurophysiology* **75**:2509–2519. DOI: https://doi.org/10.1152/jn.1996.75.6.2509, PMID: 8793760

Major G, Larkman AU, Jonas P, Sakmann B, Jack JJ. 1994. Detailed passive cable models of whole-cell recorded CA3 pyramidal neurons in rat hippocampal slices. *The Journal of Neuroscience* **14**:4613–4638 PMID: 8046439.

Mantilla CB, Zhan W-Z, Gransee HM, Prakash YS, Sieck GC. 2018. Phrenic motoneuron structural plasticity across models of diaphragm muscle paralysis. *The Journal of Comparative Neurology* **526**:2973–2983. DOI: https://doi.org/10.1002/cne.24503, PMID: 30411341

Manuel M, Iglesias C, Donnet M, Leroy F, Heckman CJ, Zytnicki D. 2009. Fast kinetics, high-frequency oscillations, and subprimary firing range in adult mouse spinal motoneurons. *The Journal of Neuroscience* **29**:11246–11256. DOI: https://doi.org/10.1523/JNEUROSCI.3260-09.2009, PMID: 19741131

Manuel M, Heckman CJ. 2011. Adult mouse motor units develop almost all of their force in the subprimary range: A new all-or-none strategy for force recruitment? *The Journal of Neuroscience* **31**:15188–15194. DOI: https://doi.org/10.1523/JNEUROSCI.2893-11.2011, PMID: 22016552

Manuel M, Chardon M, Tysseling V, Heckman CJ. 2019. Scaling of motor output, from mouse to humans. *Physiology* **34**:5–13. DOI: https://doi.org/10.1152/physiol.00021.2018, PMID: 30540233

Martínez-Silva M, Imhoff-Manuel RD, Sharma A, Heckman CJ, Shneider NA, Roselli F, Zytnicki D, Manuel M. 2018. Hypoexcitability precedes denervation in the large fast-contracting motor units in two unrelated mouse models of ALS. *eLife* **7**:e30955. DOI: https://doi.org/10.7554/eLife.30955, PMID: 29580378

Mateika JH, Essif EG, Dellorusso C, Fregosi RF. 1998. Contractile properties of human nasal dilator motor units. *Journal of Neurophysiology* **79**:371–378. DOI: https://doi.org/10.1152/jn.1998.79.1.371, PMID: 9425206

McNulty PA, Macefield VG. 2005. Intraneural microstimulation of motor axons in the study of human single motor units. *Muscle & Nerve* **32**:119–139. DOI: https://doi.org/10.1002/mus.20324, PMID: 15880485

Mcphedran AM, Wuerker RB, Henneman E. 1965. Properties of motor units in a homogeneous red muscle (soleus) of the cat. *Journal of Neurophysiology* **28**:71–84. DOI: https://doi.org/10.1152/jn.1965.28.1.71, PMID: 14244797

Mierzejewska-Krzyżowska B, Bukowska D, Taborowska M, Celichowski J. 2014. Sex differences in the number and size of motoneurons innervating rat medial gastrocnemius muscle. *Anatomia, Histologia, Embryologia* **43**:182–189. DOI: https://doi.org/10.1111/ahe.12060, PMID: 23617786

Milner-Brown HS, Stein RB, Yemm R. 1973. The orderly recruitment of human motor units during voluntary isometric contractions. *The Journal of Physiology* **230**:359–370. DOI: https://doi.org/10.1113/jphysiol.1973.sp010192, PMID: 4350770

Mitra P, Brownstone RM. 2012. An in vitro spinal cord slice preparation for recording from lumbar motoneurons of the adult mouse. *Journal of Neurophysiology* **107**:728–741. DOI: https://doi.org/10.1152/jn.00558.2011, PMID: 22031766

Moschovakis AK, Burke RE, Fyffe REW. 1991. The size and dendritic structure of HRP-labeled gamma motoneurons in the cat spinal cord. *The Journal of Comparative Neurology* **311**:531–545. DOI: https://doi.org/10.1002/cne.903110408, PMID: 1757602

Munson JB, Foehring RC, Lofton SA, Zengel JE, Sypert GW. 1986. Plasticity of medial gastrocnemius motor units following cordotomy in the cat. *Journal of Neurophysiology* **55**:619–634. DOI: https://doi.org/10.1152/jn.1986.55.4.619, PMID: 3701396

Nakanishi ST, Whelan PJ. 2010. Diversification of intrinsic motoneuron electrical properties during normal development and botulinum toxin-induced muscle paralysis in early postnatal mice. *Journal of Neurophysiology* **103**:2833–2845. DOI: https://doi.org/10.1152/jn.00022.2010, PMID: 20457856

Negro F, Yavuz ŞU, Yavuz UŞ, Farina D. 2014. Limitations of the spike-triggered averaging for estimating motor unit twitch force: A theoretical analysis. *PLOS ONE* **9**:e92390. DOI: https://doi.org/10.1371/journal.pone.0092390, PMID: 24667744

Negro F, Yavuz UŞ, Farina D. 2016. The human motor neuron pools receive a dominant slow-varying common synaptic input. *The Journal of Physiology* **594**:5491–5505. DOI: https://doi.org/10.1113/JP271748, PMID: 27151459

Nordstrom MA, Miles TS. 1990. Fatigue of single motor units in human masseter. *Journal of Applied Physiology* **68**:26–34. DOI: https://doi.org/10.1152/jappl.1990.68.1.26, PMID: 2312467

Obregón G, Ermilov LG, Wen-Zhi Z, Sieck GC, Mantilla CB. 2009. Modeling dendritic arborization based on 3D-reconstructions of adult rat phrenic motoneurons. *Revista Ingeniería Biomédica* **3**:47–54.

Olinder AL, Kernell A, Smide B. 2006. Treatment with CSII in two infants with neonatal diabetes mellitus. *Pediatric Diabetes* **7**:284–288. DOI: https://doi.org/10.1111/j.1399-5448.2006.00203.x, PMID: 17054451

Pinter MJ, Vanden Noven S. 1989. Effects of preventing reinnervation on axotomized spinal motoneurons in the cat. I. Motoneuron electrical properties. *Journal of Neurophysiology* **62**:311–324. DOI: https://doi.org/10.1152/jn.1989.62.2.311, PMID: 2769333

Powers RK, Binder MD. 2001. Input-output functions of mammalian motoneurons. *Reviews of Physiology, Biochemistry and Pharmacology* **143**:137–263. DOI: https://doi.org/10.1007/BFb0115594, PMID: 11428264

Prakash YS, Mantilla CB, Zhan WZ, Smithson KG, Sieck GC. 2000. Phrenic motoneuron morphology during rapid diaphragm muscle growth. *Journal of Applied Physiology* **89**:563–572. DOI: https://doi.org/10.1152/jappl.2000.89.2.563, PMID: 10926639

Proske U, Waite PME. 1974. Properties of types of motor units in the medial gastrochemius muscle of the cat. *Brain Research* **67**:89–101. DOI: https://doi.org/10.1016/0006-8993(74)90300-x, PMID: 4470419

Rafuse VF, Pattullo MC, Gordon T. 1997. Innervation ratio and motor unit force in large muscles: A study of chronically stimulated cat medial gastrocnemius. *The Journal of Physiology* **499 (Pt 3)**:809–823. DOI: https://doi.org/10.1113/jphysiol.1997.sp021970, PMID: 9130174

Rall W. 1957. Membrane time constant of motoneurons. *Science* **126**:454. DOI: https://doi.org/10.1126/science.126.3271.454, PMID: 13467230

Rall W. 1959. Branching dendritic trees and motoneuron membrane resistivity. *Experimental Neurology* **1**:491–527. DOI: https://doi.org/10.1016/0014-4886(59)90046-9, PMID: 14435979

Rall W. 1960. Membrane potential transients and membrane time constant of motoneurons. *Experimental Neurology* **2**:503–532. DOI: https://doi.org/10.1016/0014-4886(60)90029-7, PMID: 13739270

Rall W. 1969. Time constants and electrotonic length of membrane cylinders and neurons. *Biophysical Journal* **9**:1483–1508. DOI: https://doi.org/10.1016/S0006-3495(69)86467-2, PMID: 5352228

Rall W. 1977. Core conductor theory and cable properties of neurons. Poeter R (Ed). *The Nervous System*. American Physiological Society. p. 39–97.

Rall W, Burke RE, Holmes WR, Jack JJ, Redman SJ, Segev I. 1992. Matching dendritic neuron models to experimental data. *Physiological Reviews* **72**:S159–S186. DOI: https://doi.org/10.1152/physrev.1992.72.suppl_4.S159, PMID: 1438585

Reinking RM, Stephens JA, Stuart DG. 1975. The motor units of cat medial gastrocnemius: Problem of their categorisation on the basis of mechanical properties. *Experimental Brain Research* **23**:301–313. DOI: https://doi.org/10.1007/BF00239742, PMID: 1183507

Sasaki M. 1991. Membrane properties of external urethral and external anal sphincter motoneurones in the cat. *The Journal of Physiology* **440**:345–366. DOI: https://doi.org/10.1113/jphysiol.1991.sp018712, PMID: 1804967

Sica REP, McComas AJ. 1971. Fast and slow twitch units in a human muscle. *Journal of Neurology, Neurosurgery, and Psychiatry* **34**:113–120. DOI: https://doi.org/10.1136/jnnp.34.2.113, PMID: 4255199

Solsona C, Innocenti B, Fernández JM. 1998. Regulation of exocytotic fusion by cell inflation. *Biophysical Journal* **74**:1061–1073. DOI: https://doi.org/10.1016/S0006-3495(98)74030-5, PMID: 9533718

Song ZM, Hu J, Rudy B, Redman SJ. 2006. Developmental changes in the expression of calbindin and potassium-channel subunits Kv3.1b and Kv3.2 in mouse Renshaw cells. *Neuroscience* **139**:531–538. DOI: https://doi.org/10.1016/j.neuroscience.2005.12.048, PMID: 16460880

Spruston N, Johnston D. 1992. Perforated patch-clamp analysis of the passive membrane properties of three classes of hippocampal neurons. *Journal of Neurophysiology* **67**:508–529. DOI: https://doi.org/10.1152/jn.1992.67.3.508, PMID: 1578242

Stephens JA, Stuart DG. 1975. The motor units of cat medial gastrocnemius: speed-size relations and their significance for the recruitment order of mortor units. *Brain Research* **91**:177–195. DOI: https://doi.org/10.1016/0006-8993(75)90542-9, PMID: 1164670

Stephens JA, Usherwood TP. 1977. The mechanical properties of human motor units with special reference to their fatiguability and recruitment threshold. *Brain Research* **125**:91–97. DOI: https://doi.org/10.1016/0006-8993(77)90361-4, PMID: 851876

Sukhorukov VL, Arnold WM, Zimmermann U. 1993. Hypotonically induced changes in the plasma membrane of cultured mammalian cells. *The Journal of Membrane Biology* **132**:27–40. DOI: https://doi.org/10.1007/BF00233049, PMID: 8459447

Swett JE, Wikholm RP, Blanks RH, Swett AL, Conley LC. 1986. Motoneurons of the rat sciatic nerve. *Experimental Neurology* **93**:227–252. DOI: https://doi.org/10.1016/0014-4886(86)90161-5, PMID: 3732460

Taylor AM, Steege JW, Enoka RM. 2002. Motor-unit synchronization alters spike-triggered average force in simulated contractions. *Journal of Neurophysiology* **88**:265–276. DOI: https://doi.org/10.1152/jn.2002.88.1.265, PMID: 12091552

Teeter C, Iyer R, Menon V, Gouwens N, Feng D, Berg J, Szafer A, Cain N, Zeng H, Hawrylycz M, Koch C, Mihalas S. 2018. Generalized leaky integrate-and-fire models classify multiple neuron types. *Nature Communications* **9**:1–15. DOI: https://doi.org/10.1038/s41467-017-02717-4, PMID: 29459723

Thomas CK, Johansson RS, Westling G, Bigland-Ritchie B. 1990. Twitch properties of human thenar motor units measured in response to intraneural motor-axon stimulation. *Journal of Neurophysiology* **64**:1339–1346. DOI: https://doi.org/10.1152/jn.1990.64.4.1339, PMID: 2258751

Thomas CK, Bigland-Richie B, Johansson RS. 1991. Force-frequency relationships of human thenar motor units. *Journal of Neurophysiology* **65**:1509–1516. DOI: https://doi.org/10.1152/jn.1991.65.6.1509, PMID: 1875259

Thurbon D, Lüscher H-R, Hofstetter T, Redman SJ. 1998. Passive electrical properties of ventral horn neurons in rat spinal cord slices. *Journal of Neurophysiology* **79**:2485–2502. DOI: https://doi.org/10.1152/jn.1998.79.5.2485, PMID: 9722433

Tötösy de Zepetnek JE, Zung HV, Erdebil S, Gordon T. 1992. Innervation ratio is an important determinant of force in normal and reinnervated rat tibialis anterior muscles. *Journal of Neurophysiology* **67**:1385–1403. DOI: https://doi.org/10.1152/jn.1992.67.5.1385, PMID: 1597721

Turkin VV, O'Neill D, Jung R, Iarkov A, Hamm TM. 2010. Characteristics and organization of discharge properties in rat hindlimb motoneurons. *Journal of Neurophysiology* **104**:1549–1565. DOI: https://doi.org/10.1152/jn.00379.2010, PMID: 20592119

Ulfhake B, Kellerth JO. 1981. A quantitative light microscopic study of the dendrites of cat spinal alpha-motoneurons after intracellular staining with horseradish peroxidase. *The Journal of Comparative Neurology* **202**:571–583. DOI: https://doi.org/10.1002/cne.902020409, PMID: 7298916

Ulfhake B, Kellerth JO. 1984. Electrophysiological and morphological measurements in cat gastrocnemius and soleus alpha-motoneurones. *Brain Research* **307**:167–179. DOI: https://doi.org/10.1016/0006-8993(84)90471-2, PMID: 6466992

Ulfhake B, Cullheim S. 1988. Postnatal development of cat hind limb motoneurons. III: Changes in size of motoneurons supplying the triceps surae muscle. *The Journal of Comparative Neurology* **278**:103–120. DOI: https://doi.org/10.1002/cne.902780107, PMID: 3209749

Van Cutsem M, Feiereisen P, Duchateau J, Hainaut K. 1997. Mechanical properties and behaviour of motor units in the tibialis anterior during voluntary contractions. *Canadian Journal of Applied Physiology = Revue Canadienne de Physiologie Appliquee* **22**:585–597. DOI: https://doi.org/10.1139/h97-038, PMID: 9415831

Vult von Steyern F, Martinov V, Rabben I, Njå A, de Lapeyrière O, Lømo T. 1999. The homeodomain transcription factors Islet 1 and HB9 are expressed in adult alpha and gamma motoneurons identified by selective retrograde tracing. *The European Journal of Neuroscience* **11**:2093–2102. DOI: https://doi.org/10.1046/j.1460-9568.1999.00631.x, PMID: 10336678

Wuerker RB, Mcphedran AM, Henneman E. 1965. Properties of motor units in a heterogeneous pale muscle (m. gastrocnemius) of the cat. *Journal of Neurophysiology* **28**:85–99. DOI: https://doi.org/10.1152/jn.1965.28.1.85, PMID: 14244798

Yemm R. 1977. The orderly recruitment of motor units of the masseter and temporal muscles during voluntary isometric contraction in man. *The Journal of Physiology* **265**:163–174. DOI: https://doi.org/10.1113/jphysiol.1977.sp011710, PMID: 850157

Young JL, Mayer RF. 1982. Physiological alterations of motor units in hemiplegia. *Journal of the Neurological Sciences* **54**:401–412. DOI: https://doi.org/10.1016/0022-510x(82)90203-9, PMID: 7097310

Zengel JE, Reid SA, Sypert GW, Munson JB. 1985. Membrane electrical properties and prediction of motor-unit type of medial gastrocnemius motoneurons in the cat. *Journal of Neurophysiology* **53**:1323–1344. DOI: https://doi.org/10.1152/jn.1985.53.5.1323, PMID: 3839011

Zwaagstra B, Kernell D. 1980. The duration of after-hyperpolarization in hindlimb alpha motoneurones of different sizes in the cat. *Neuroscience Letters* **19**:303–307. DOI: https://doi.org/10.1016/0304-3940(80)90278-5, PMID: 7052536

Zwaagstra B, Kernell D. 1981. Sizes of soma and stem dendrites in intracellularly labelled alpha-motoneurones of the cat. *Brain Research* **204**:295–309. DOI: https://doi.org/10.1016/0006-8993(81)90590-4, PMID: 7459633
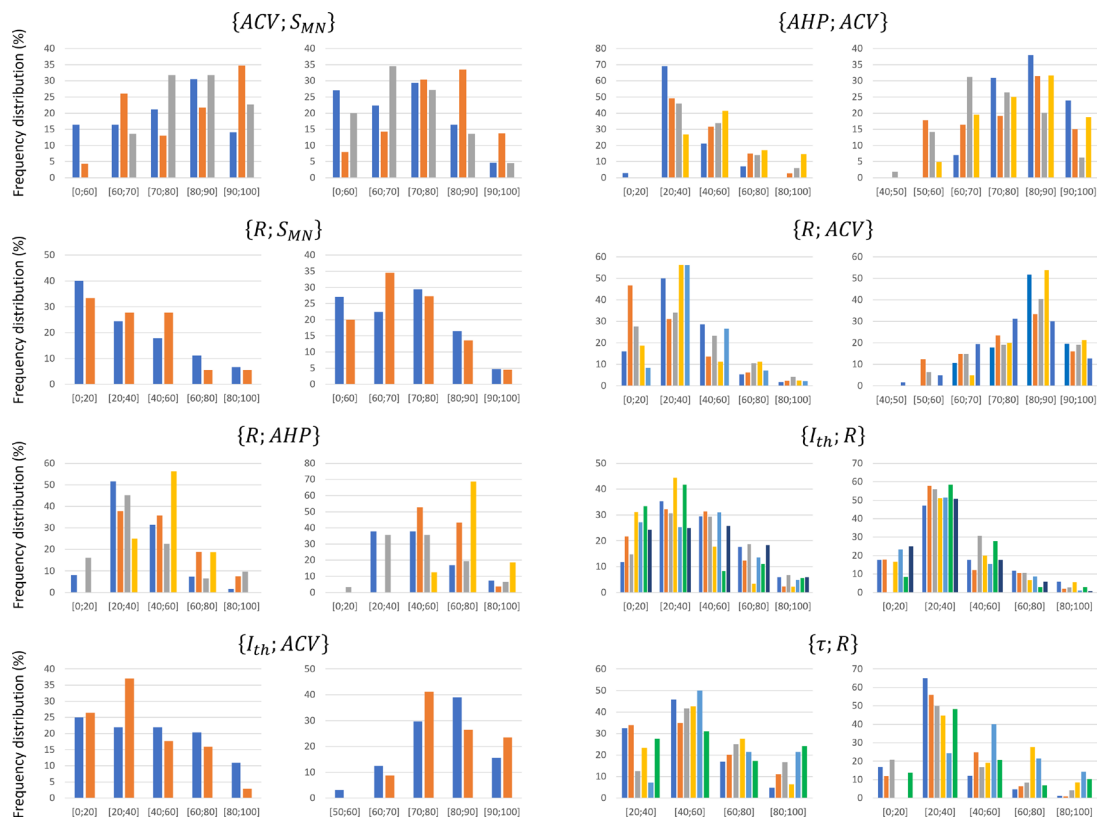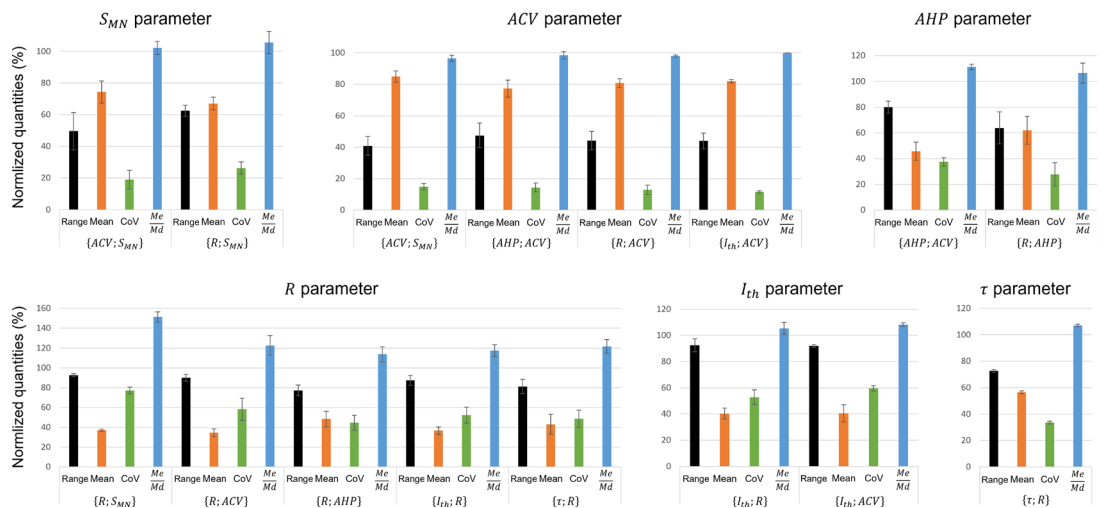
Appendix 1

Inter-study data variability

Inter-study variability greater than the threshold defined in 'Methods' was observed in three, two, and four property distributions for the metrics range, mean, and CoV metrics, respectively. Indeed, sensibly different ranges of property values were observed to be reported between studies of the $\{ACV; S_{MN}\}$, $\{AHP; ACV\}$, and $\{R; AHP\}$ datasets for the S_{MN}, ACV, and AHP properties, respectively, with $sd_g \in [10; 15]$ % and/or $\frac{sd_g}{mean_g} \in [0.15; 0.33]$. Also, the studies of the $\{R; AHP\}$ and $\{\tau; R\}$ datasets returned some variability in the mean of the reported data for properties AHP and R, respectively, with $sd_g \in [10; 11]$ % and/or $\frac{sd_g}{mean_g} \in [0.15; 0.23]$. The $\{ACV; S_{MN}\}$, $\{R; ACV\}$, and $\{R; AHP\}$ global datasets showed variable data dispersion around the mean for properties S_{MN}, R and ACV, and AHP, respectively, with $sd_g \in [10; 11]$ % and/or $\frac{sd_g}{mean_g} \in [0.15; 0.30]$.

Discussion on the potential underestimation of q_S^E

The minimum and maximum values of S_{neuron} and D_{soma} reported in *Appendix 1—table 1* may underestimate the true distribution of MN sizes in an MN pool for several reasons, and thus underestimate the true value of q_S^E. First, the studies reported in *Appendix 1—table 1* investigated MN populations of small size, so that the largest and smallest MNs of the investigated MN pools may not have been systematically identified and measured. Also, dendritic labelling by staining may only identify dendrites up to the third dendritic branch (*Issa et al., 2010*; *Brandenburg et al., 2018*) and full dendritic trees may not be identified, thus underestimating S_{neuron} for the largest MNs that exhibit the highest dendritic tree complexity (*Brandenburg et al., 2020*). Finally, the distribution of gamma- and alpha-MN sizes is typically bimodal and the size distributions of the two populations are reported to overlap (*Moschovakis et al., 1991*; *Vult von Steyern et al., 1999*; *Friese et al., 2009*; *Deardorff et al., 2013*). However, most studies reported in *Appendix 1—table 1* identify the alpha MNs from the gamma MNs by visually splitting the bimodal distributions of MN sizes in two independent domains (*Donselaar et al., 1986*; *Ishihara et al., 2001*), thus neglecting the overlap. Similarly, some studies identify as gamma MNs any MN showing an axonal conduction velocity typically less than $\sim 60 m \cdot s^{-1}$ (*Zwaagstra and Kernell, 1980*; *Ulfhake and Kellerth, 1984*). These approaches lead to overestimating the lower limit for the reported D_{soma} and S_{neuron} values. Consequently, true ranges in MN sizes may be larger than the theoretical ones reported in *Appendix 1—table 1*. A similar comment can be made for the electrophysiological properties reported in *Appendix 1—table 2*. However, the $q_S^E = 2.4$-fold range obtained for cats is consistent with the fold ranges obtained from rat and mouse data for D_{soma}, as reported in *Appendix 1—table 1*, while it underestimates the 4.4-fold range in S_{neuron} values observed in mice. *Appendix 1—table 1* finally shows that typical cat MN sizes are larger than in rats and mice, as reviewed by *Manuel et al., 2019*.

Appendix 1—figure 1. Density histograms of the data distributions reported in the experimental studies included in the global datasets. Depending on the typical range over which each property spans, the distributions are divided in steps of 10 or 20%. The frequency distribution is provided in percentage of the total number of reported data points in a study. Different studies are displayed with different colours in each graph. For each dataset $\{A; B\}$, the frequency distributions of property A and B are provided in the left and right plot, respectively.
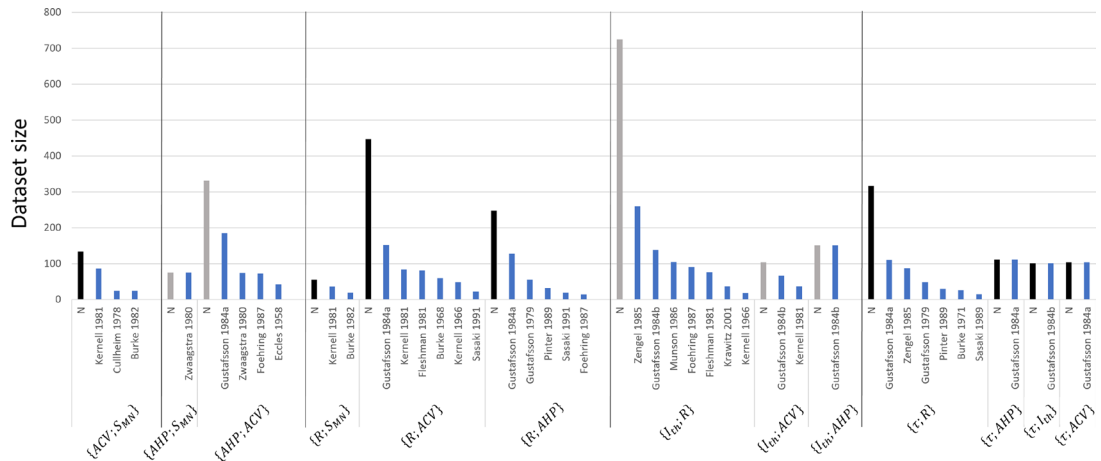

Appendix 1—figure 2. Assessment of data variability between the experimental studies that constitute the eight global datasets that include at least two experimental studies. For each experimental study included in the global dataset $\{A; B\}$, the range, mean, coefficient of variation ($CoV = \frac{standard\ deviation}{Mean}$), and the ratio $\frac{Me}{Md} = \frac{Mean}{Median}$ of the experimental A values measured in this study were computed. Then, the average (bars) and standard deviation (error bars) across experimental studies of these four metrics (range, mean, CoV, $\frac{Me}{Md}$) were calculated for each global dataset independently. For example, the first bar in the 'S_{MN} parameter' plot represents the average across three studies (**Kernell and Zwaagstra, 1981**; **Cullheim, 1978**; **Burke et al., 1982**) of the range of S_{MN}

values reported in these studies, for the global dataset $\{ACV; S_{MN}\}$. The computed standard deviations (error bars) express for each global dataset the inter-study variability of (1) the length of the identified bandwidth of the motoneuron (MN) pool (range metric), (2) the spread of values around the mean (CoV metric), (3) the skewness of the distributions, and (4) whether the distributions from different studies are centred (mean metric). A global dataset $\{A; B\}$ reporting narrow error bars for parameter A for the four metrics infers that the experimental studies constituting this dataset measured similar distributions of property A.

Appendix 1—figure 3. Distribution of the size of the experimental datasets constituting the global datasets for assessment of the variability in the input data. The histogram is divided between global datasets (half vertical lines), grouped as final size-dependent datasets (full vertical lines). For each global dataset, the total number of data points is reported (label: 'N'), while the size of the constitutive experimental studies is reported in decreasing order.
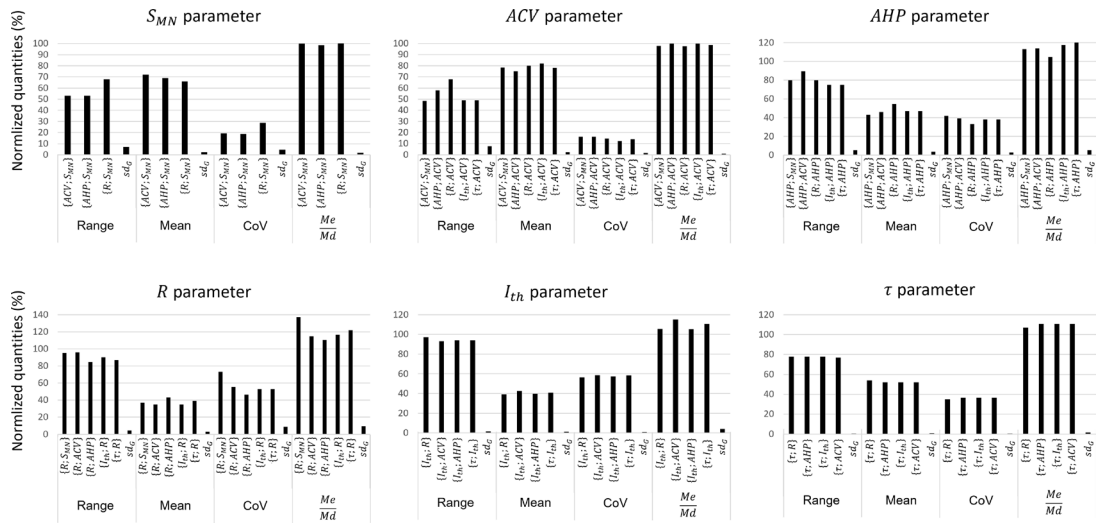
Appendix 1—figure 4. Assessment of data variability between the global datasets. This figure compares the distributions of the S_{MN}, ACV, AHP, R, I_{th}, and τ properties between the normalized global datasets built in this study. For each property, the range, mean, coefficient of variation ($oV = \frac{standard\ deviation}{Mean}$), and the ratio $\frac{Me}{Md} = \frac{Mean}{Median}$ of its distribution in a global dataset is compared to the other global datasets it appears in. For each property, the standard deviation sd_G between global datasets of these four metrics is computed. A low sd_G value reflects the low variability of the property distribution between global datasets.

Appendix 1—table 1. r^2 values obtained for each experimental dataset $\{A; B\}$ when performing a linear regression analysis on $\{A; B\}$ directly ('Linear') and on the $ln(A) - ln(B)$ ('Power') and $ln(A) - B$ ('Exponential') transformations of $\{A; B\}$.

The r^2 values returned by the three types of regression cannot be directly compared to estimate the best model. However, the power fit returned $r^2 > 0.5$ for relatively more experimental datasets than the linear and exponential fits.

	Studies	Linear	Power	Exponential
	Cullheim, 1978	0.42	0.45	0.43
	Kernell and Zwaagstra, 1981	0.62	0.63	0.6
$\{ACV; S_{MN}\}$	*Burke et al., 1982*	0.23	0.26	0.24
$\{AHP; S_{MN}\}$	*Zwaagstra and Kernell, 1980*	0.33	0.37	0.35
	Eccles et al., 1958b	0.53	0.54	0.54
	Zwaagstra and Kernell, 1980	0.42	0.44	0.42
	Gustafsson and Pinter, 1984a	0.71	0.68	0.7
$\{AHP; ACV\}$	*Foehring et al., 1987*	0.15	0.14	0.14
	Kernell and Zwaagstra, 1981	0.68	0.71	0.7
$\{R; S_{MN}\}$	*Burke et al., 1982*	0.41	0.5	0.46
	Kernell, 1966	0.70	0.65	0.64
	Burke, 1968	0.28	0.31	0.31
	Kernell and Zwaagstra, 1981	0.68	0.71	0.71
	Fleshman et al., 1981	0.3	0.21	0.2
	Gustafsson and Pinter, 1984a	0.45	0.44	0.42
$\{R; ACV\}$	*Sasaki, 1991*	0.68	0.68	0.66
	Gustafsson, 1979	0.43	0.41	0.42
	Gustafsson and Pinter, 1984a	0.71	0.68	0.67
	Foehring et al., 1987	0.33	0.32	0.33
	Pinter and Vanden Noven, 1989	0.66	0.53	0.59
$\{R; AHP\}$	*Sasaki, 1991*	0.57	0.49	0.52
	Kernell, 1966	0.52	0.52	0.68
	Fleshman et al., 1981	0.28	0.34	0.38
	Gustafsson and Pinter, 1984b	0.63	0.83	0.83
	Zengel et al., 1985	0.49	0.6	0.62
	Munson et al., 1986	0.34	0.42	0.47
	Foehring et al., 1987	0.34	0.47	0.47
$\{I_{th}; R\}$	*Krawitz et al., 2001*	0.32	0.49	0.44
	Kernell and Zwaagstra, 1981	0.23	0.24	0.24
$\{I_{th}; ACV\}$	*Gustafsson and Pinter, 1984b*	0.4	0.52	0.5

Appendix 1—table 1 Continued on next page

Appendix 1—table 1 Continued

	Studies	Linear	Power	Exponential
$\{I_{th}; AHP\}$	Gustafsson and Pinter, 1984b	0.55	0.72	0.69
$\{C; R\}$	Gustafsson and Pinter, 1984a	0.55	0.57	0.57
$\{C; I_{th}\}$	Gustafsson and Pinter, 1984a	0.23	0.34	0.24
$\{C; AHP\}$	Gustafsson and Pinter, 1984a	0.25	0.26	0.26
$\{C; ACV\}$	Gustafsson and Pinter, 1984a	0.17	0.22	0.19
	Burke and ten Bruggencate, 1971	0.04	0.07	0.03
	Gustafsson, 1979	0.6	0.63	0.61
	Gustafsson and Pinter, 1984a	0.63	0.69	0.59
	Zengel et al., 1985	0.39	0.33	0.36
	Pinter and Vanden Noven, 1989	0.65	0.69	0.62
$\{\tau; R\}$	Sasaki, 1991	0.68	0.72	0.64
$\{\tau; I_{th}\}$	Gustafsson and Pinter, 1984b	0.63	0.59	0.57
$\{\tau; ACV\}$	Gustafsson and Pinter, 1984a	0.69	0.76	0.76
$\{\tau; AHP\}$	Gustafsson and Pinter, 1984a	0.34	0.32	0.31

Appendix 1—table 2. Mathematical empirical normalized relationships between the motoneuron (MN) properties D_{soma}, R, C, τ, I_{th}, AHP, and ACV. Each column provides the relationships between one and the six other MN properties. All constants and properties are normalized up to a theoretical 100% maximum value. To scale the normalized relationships $A = k \cdot B^c$ for a specific mammalian species, the normalized intercept k must be scaled with a pair of values for properties A and B obtained from the same motoneuron in that species.

	D_{soma}	R	C	τ	I_{th}	AHP	ACV
D_{soma}		$R = \frac{9.6 \cdot 10^5}{D_{soma}^{2.4}}$	$C = 1.2 \cdot D_{soma}$	$\tau = \frac{2.6 \cdot 10^4}{D_{soma}^{1.5}}$	$I_{th} = 9.0 \cdot 10^{-4} \cdot D_{soma}^{2.5}$	$AHP = \frac{2.5 \cdot 10^4}{D_{soma}^{1.5}}$	$ACV = 4.0 \cdot D_{soma}^{0.7}$
R	$D_{soma} = \frac{2.9 \cdot 10^2}{R^{0.4}}$		$C = \frac{2.7 \cdot 10^2}{R^{0.4}}$	$\tau = 5.8 \cdot R^{0.6}$	$I_{th} = \frac{1.5 \cdot 10^3}{R}$	$AHP = 4.7 \cdot R^{0.6}$	$ACV = \frac{2.0 \cdot 10^2}{R^{0.3}}$
C	$D_{soma} = 8.6 \cdot 10^{-1} \cdot C$	$R = \frac{1.4 \cdot 10^6}{C^{2.5}}$		$\tau = \frac{3.3 \cdot 10^4}{C^{1.5}}$	$I_{th} = 6.2 \cdot 10^{-4} \cdot C^{2.6}$	$AHP = \frac{3.1 \cdot 10^4}{C^{1.6}}$	$ACV = 3.6 \cdot C^{0.7}$
τ	$D_{soma} = \frac{9.5 \cdot 10^2}{\tau^{0.7}}$	$R = 5.6 \cdot 10^{-2} \cdot \tau^{1.6}$	$C = \frac{8.5 \cdot 10^2}{\tau^{0.7}}$		$I_{th} = \frac{2.9 \cdot 10^4}{\tau^{1.7}}$	$AHP = 7.8 \cdot 10^{-1} \cdot \tau$	$ACV = \frac{4.6 \cdot 10^2}{\tau^{0.5}}$
I_{th}	$D_{soma} = 1.6 \cdot 10^1 \cdot I_{th}^{0.4}$	$R = \frac{1.1 \cdot 10^3}{I_{th}}$	$C = 1.7 \cdot 10^1 \cdot I_{th}^{0.4}$	$\tau = \frac{4.2 \cdot 10^2}{I_{th}^{0.6}}$		$AHP = \frac{3.7 \cdot 10^2}{I_{th}^{0.6}}$	$ACV = 2.7 \cdot 10^1 \cdot I_{th}^{0.3}$
AHP	$D_{soma} = \frac{8.1 \cdot 10^2}{AHP^{0.7}}$	$R = 8.4 \cdot 10^{-2} \cdot AHP^{1.6}$	$C = \frac{7.3 * 10^2}{AHP^{0.6}}$	$\tau = 1.3 \cdot AHP$	$I_{th} = \frac{1.9 * 10^4}{AHP^{1.7}}$		$ACV = \frac{4.1 \cdot 10^2}{AHP^{0.5}}$
ACV	$D_{soma} = 1.4 \cdot 10^{-1} \cdot ACV^{1.4}$	$R = \frac{1.2 \cdot 10^8}{ACV^{3.5}}$	$C = 1.7 \cdot 10^{-1} \cdot ACV^{1.4}$	$\tau = \frac{5.0 \cdot 10^5}{ACV^{2.1}}$	$I_{th} = 5.9 \cdot 10^{-6} \cdot ACV^{3.6}$	$AHP = \frac{5.0 \cdot 10^5}{ACV^{2.2}}$	

Appendix 1—table 3. Typical ranges of physiological values for D_{soma} and S_{neuron} in cat rat and mouse species.

S_{MN} is found to vary over an average $q_S^E = 2.4$-fold range, which sets the amplitude of the theoretical ranges. Absolute {min; max} reports the minimum and maximum values retrieved in the reference studies for D_{soma} and S_{neuron}, while average {min; max} is obtained as the average across reference studies of minimum and maximum values retrieved per study.

	Property	Unit	Absolute {min;max}	Average {min; max}	q_S^E	Reference studies	Theoretical range
Cat	D_{soma}	[µm]	$\{25.0; 90.0\}$	$\{36.7; 75.5\}$	2.2	*Kernell, 1966; Cullheim, 1978; Zwaagstra and Kernell, 1980; Kernell and Zwaagstra, 1981; Ulfhake and Kellerth, 1981; Zwaagstra and Kernell, 1981; Burke et al., 1982; Donselaar et al., 1986; Destombes et al., 1992*	[33; 79]
	S_{neuron}	[mm²]	$\{0.08; 0.64\}$	$\{0.17; 0.45\}$	2.7	*Barrett and Crill, 1974; Ulfhake and Kellerth, 1981; Burke et al., 1982; Ulfhake and Kellerth, 1984; Ulfhake and Cullheim, 1988; Moschovakis et al., 1991*	[0.18; 0.44]
Rat	D_{soma}	[µm]	$\{17.5; 66.0\}$	$\{23.9; 55.7\}$	2.4	*Swett et al., 1986; Vult von Steyern et al., 1999; Copray and Kernell, 2000; Ishihara et al., 2001; Deardorff et al., 2013; Mierzejewska-Krzyżowska et al., 2014*	
Mouse	D_{soma}	[µm]	$\{14.0; 35.0\}$	$\{14.0; 35.0\}$	2.5	*Vult von Steyern et al., 1999*	
	S_{neuron}	[mm²]	$\{0.01; 0.08\}$	$\{0.01; 0.06\}$	4.4	*Amendola and Durand, 2008; Brandenburg et al., 2020*	

Appendix 1—table 4. Typical ranges of physiological values for the motoneuron (MN) properties R, R_m, C, τ, I_{th}, AHP, and ACV.

As described in 'Methods', q_A^E is the average among reference studies of the ratios of minimum and maximum values; the properties experimentally vary over a q_A^E-fold range. This ratio compares with the theoretical ratio $q_A^T = \left(q_S^E\right)^{|c|}$ (with c taken from **Table 3**), which sets the amplitude of the theoretical ranges. Absolute and average {min; max} are obtained as described in the main sections.

MN property	Unit	Absolute exp {min;max}	Average exp {min; max}	q_A^E	Reference studies	q_A^T	$\frac{q_A^E}{q_A^T}$	Theoretical range
R	[MΩ]	$\{0.2; 8.1\}$	$\{0.4; 4.0\}$	10.9	*Kernell, 1966; Burke, 1968; Burke and ten Bruggencate, 1971; Barrett and Crill, 1974; Gustafsson, 1979; Kernell and Zwaagstra, 1981; Fleshman et al., 1981; Burke et al., 1982; Ulfhake and Kellerth, 1984; Gustafsson and Pinter, 1984a; Zengel et al., 1985; Foehring et al., 1986; Munson et al., 1986; Foehring et al., 1987; Sasaki, 1991; Krawitz et al., 2001*	8.4	1.3	$[0.5; 4.0]$
C	[nF]	$\{2.2; 8.5\}$	$\{2.2; 8.5\}$	3.9	*Gustafsson and Pinter, 1984a; Gustafsson and Pinter, 1985*	2.3	1.6	$[3.2; 7.5]$
τ	[ms]	$\{2.0; 14.2\}$	$\{2.9; 10.2\}$	3.5	*Burke and ten Bruggencate, 1971; Barrett and Crill, 1974; Gustafsson, 1979; Ulfhake and Kellerth, 1984; Gustafsson and Pinter, 1984a; Gustafsson and Pinter, 1985; Sasaki, 1991*	3.7	0.9	$[2.8; 10.3]$
I_{th}	[nA]	$\{1.7; 52.7\}$	$\{2.3; 36.6\}$	16.3	*Fleshman et al., 1981; Kernell and Monster, 1981; Ulfhake and Kellerth, 1984; Gustafsson and Pinter, 1984b; Zengel et al., 1985; Foehring et al., 1986; Munson et al., 1986; Foehring et al., 1987; Krawitz et al., 2001*	9.1	1.8	$[3.9; 35.0]$
AHP	[ms]	$\{10.6; 266.6\}$	$\{44.2; 158.7\}$	4.1	*Eccles et al., 1957; Gustafsson, 1979; Dum and Kennedy, 1980; Zwaagstra and Kernell, 1980; Ulfhake and Kellerth, 1984; Gustafsson and Pinter, 1984a; Zengel et al., 1985; Foehring et al., 1987; Sasaki, 1991*	3.8	1.1	$[42.6; 160.2]$
ACV	[m·s⁻¹]	$\{51.1; 127.2\}$	$\{65.3; 114.8\}$	1.8	*Eccles et al., 1957; Mcphedran et al., 1965; Kernell, 1966; Appelberg and Emonet-Dénand, 1967; Burke, 1968; Barrett and Crill, 1974; Proske and Waite, 1974; Bagust, 1974; Stephens and Stuart, 1975; Cullheim, 1978; Dum and Kennedy, 1980; Zwaagstra and Kernell, 1980; Kernell and Zwaagstra, 1981; Fleshman et al., 1981; Glenn and Dement, 1981; Burke et al., 1982; Gustafsson and Pinter, 1984a; Zengel et al., 1985; Foehring et al., 1986; Foehring et al., 1987*	2.3	0.8	$[63.5; 116.6]$

Appendix 1—table 5. Validation of the cat relationships (Table 4) against rat and mouse data. nME, normalized maximum error; nRMSE, normalized root mean square error; r^2_{pred}, coefficient of determination between experimental and predicted quantities; r^2_{exp}, coefficient of determination of the power trendline directly fitted to the experimental data.

Animal	Dataset	Reference studies	nME (%)	nRMSE (%)	r^2_{pred}	r^2_{exp}
Rat	$\{I_{th}; R\}$	*Gardiner, 1993*; *Bakels and Kernell, 1993*; *Lee and Heckman, 1998*; *Button et al., 2008*; *Turkin et al., 2010*; *Krutki et al., 2015*	352	16	0.53	0.54
	$\{I_{th}; R\}$	*Delestrée et al., 2014*; *Martínez-Silva et al., 2018*; *Huh et al., 2021*	385	16	0.46	0.46
	$\{\tau; R\}$	*Manuel et al., 2009*	1219	168	0.35	0.40
Mouse	$\{C; R\}$	*Manuel et al., 2009*	1915	98	0.38	0.38